JOURNAL OF PROPULSION AND POWER
Vol. 26, No. 3, May–June 2010

Analysis of Gas-Dynamic Effects in Explosively Actuated Valves

Blaise H. Paul* and Keith A. Gonthier†
Louisiana State University, Baton Rouge, Louisiana 70803

DOI: 10.2514/1.43190

A quasi-one-dimensional model is formulated to assess unsteady gas dynamics occurring within axisymmetric explosively actuated valves. The model accounts for pressure-dependent explosive burn within an actuator, compressible product-gas flow through a narrow port connecting the actuator to a gas expansion chamber, and piston motion due to the combined effects of gas-dynamic forces within the expansion chamber and structural deformation forces between the piston and valve bore. The initial boundary-value problem is posed in terms of generalized coordinates to facilitate numerical computations on a domain that volumetrically expands due to combustion and piston motion. Predictions for a baseline configuration that is representative of a conventional valve indicate that gas-dynamic waves do not result in irregular operation, implying that spatially homogeneous models may be adequate for describing its performance. However, small changes in valve geometry and explosive mass can produce large variations in gas-dynamic fields that significantly affect both the magnitude and frequency of the pyrotechnic shock transmitted to the valve's supporting structure. Port diameter is shown to control the rates of explosive energy release and acoustic energy transport, which can significantly affect piston motion and stroke time.

I. Introduction

MANY solid explosives rapidly produce large amounts of gas when burned; as such, they are routinely used as self-contained, high-pressure gas sources to remotely actuate devices such as pin pullers, valves, thrusters, and cable cutters [1–4]. These devices often perform critical functions within the aerospace industry, including chute deployment, emergency jettison of components, and fuel flow control [5–7]. Miniaturization of explosively actuated devices has also been explored to accommodate smaller systems that reduce payload mass [8,9]. For example, the work of Rossi et al. [10–12] has recently focused on the development of microthrusters for satellite attitude control. Historically, assessing device performance has been time-consuming, expensive, and heavily based on empiricism [13]. Although experiments are necessary to observe actual device behavior, computational modeling can facilitate interpretation of experiments and assist in the design of new devices.

Assessing the performance of explosively actuated valves requires understanding the complex interplay between pressure-dependent combustion, mass and acoustic energy transport, structural mechanics, and device geometry. An overall objective of this work is to formulate a comprehensive model that can be used to quickly examine the effects of geometric, structural, and energetic material modifications on the power-producing capability and performance of explosively actuated devices. To this end, we focus on describing the operation and performance of a conventional valve, but emphasize that our model can be easily adapted and applied to other devices such as pin pullers and cable cutters. Here, *performance* collectively refers to quantities that are typically used to characterize valve operation, including its pressure history, stroke time, and pyrotechnic shock.

The axisymmetric valve modeled in this work is shown in Fig. 1 in both its prefired and postfired configurations. Representative valve dimensions are indicated in the figure; other relevant dimensions are given later in this paper. The purpose of this valve is to enable flow of stored nitrogen gas through a transfer conduit at a desired time. The valve is driven by the combustion of 150 mg of the solid explosive HMX ($C_4H_8N_8O_8$) contained within a small actuator cartridge that is threaded into the device directly above the product-gas expansion chamber. Combustion of the explosive, which is initiated by an embedded hot wire, produces a mixture of high-temperature gases that rapidly pressurize the actuator volume. The explosive and combustion products are initially sealed within the actuator by a metal burst disc that facilitates ignition and subsequent combustion by allowing for pressure buildup before rupturing. The burst disc ruptures when the pressure within the actuator exceeds a critical value ($\approx$55 MPa), enabling the flow of product gases (and possibly some unreacted explosive) through a narrow actuator port (3.8 mm diameter) and into the expansion chamber, where it exerts a net axial force on the open end of the piston (8.0 g mass), pushing it into the valve bore. This piston motion induces elastic–plastic deformation of both the initially tapered, hollow, piston skirt and the confining valve bore, resulting in significant resistance forces between these components, due to mechanical interference. The cutter, attached to the closed bottom end of the piston, penetrates the diaphragm as the moving piston is brought to rest by contact with the stops. Valve operation is complete approximately 90 μs following ignition as stored nitrogen gas flows through the newly created opening into the gas transfer conduit.

Several models have been developed to describe phenomena associated with the operation of pyrotechnically and explosively actuated devices. Notable models include those of Ng and Kwon [14] and Jones et al. [15] applied to valves, those of Kuo and Goldstein [16] and Gonthier and Powers [17] applied to pin pullers, and those of Butler et al. [18] and Vorozhtsov et al. [19] applied to airbag systems. Most relevant to this study is the model recently formulated by Braud et al. [20], which describes the coupled, time-dependent, system-level response of explosively actuated valves. Their model accounts for burning of solid explosive to form product gas within an actuator, transport of product gas from the actuator to an expansion chamber, and insertion of an initially tapered piston into a constant diameter bore by gas pressure within the expansion chamber. Many of these models assume that acoustic time scales are much smaller than the device operation time, which results in time-dependent, spatially homogeneous, thermodynamic fields that can be described by a system of ordinary differential equations (ODEs). As such, these models are incapable of predicting temporal and spatial fluctuations in pressure arising from acoustic-wave interactions within product gases and their effect on explosive combustion, piston motion, and pyrotechnic shock.

Received 12 January 2009; revision received 13 November 2009; accepted for publication 11 January 2010.

*Graduate Research Assistant, Mechanical Engineering Department.
†Associate Professor, Mechanical Engineering Department; gonthier@me.lsu.edu (Corresponding Author).

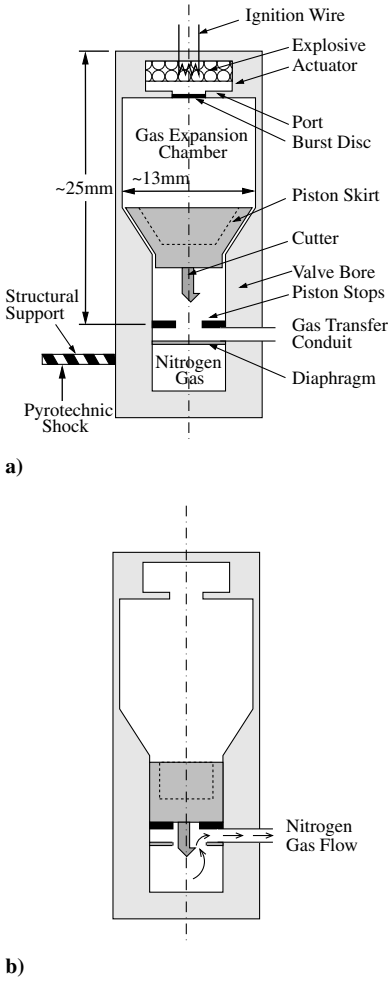

Fig. 1 Schematic of the explosively actuated nitrogen cartridge valve in a) prefired and b) postfired configurations (drawing is not to scale).

The potential need for a gas-dynamic analysis is established by comparing representative acoustic times with the device operation time. For example, the nitrogen cartridge valve is characterized by the actuator and expansion-chamber lengths L_a and L_{ec}, which define longitudinal acoustic time scales $\tau_a = L_a/c_a$ and $\tau_{\text{ec}} = L_{\text{ec}}/c_{\text{ec}}$, respectively, where c_a and c_{ec} are representative acoustic-wave speeds. If the valve operation time is given by τ_v, then spatial nonequilibrium effects induced by wave propagation are unimportant for $\tau/\tau_v \ll 1$, where τ is the acoustic time scale. For valves considered in this study, $L_a \approx 5$ mm, $L_{\text{ec}} \approx 20$ mm, $c_a \approx c_{\text{ec}} \approx 1.29$ mm/μs, and $\tau_v \approx 90$ μs. Therefore, $\tau_a \approx 3.9$ μs, $\tau_{\text{ec}} \approx 15.5$ μs, $\tau_a/\tau_v \approx 0.043$, and $\tau_{\text{ec}}/\tau_v \approx 0.172$. These estimates indicate that longitudinal-wave propagation may influence device performance, particularly within the expansion chamber. Lateral-wave-propagation effects may also be important, because the device diameter is comparable with its length. Here, we focus only on describing leading-order effects of transverse waves based on a quasi-one-dimensional (quasi-1-D) formulation; a rigorous multi-dimensional gas-dynamic analysis will be addressed by our future work. Noteworthy is the analysis performed by Lee [21], which demonstrated that one-dimensional (1-D) gas-dynamic waves can affect the performance of small explosively actuated valves. Though Lee's work accounted for gas–wall friction and heat transfer within a simple valve configuration and for volume change induced by piston motion, it did not account for device cross-sectional area variations or the effect of gas-dynamic waves on explosive burn. Gas-pressure fields are of specific interest, because explosive burn is largely pressure-dependent.

During actuation, gas-dynamic pressure waves within the actuator and expansion chamber generate large-amplitude, high-frequency stress waves within the device's mechanical components, which collectively transmit a pyrotechnic shock to the supporting structure. It is important to consider pyrotechnic shock in both the design and selection of a device for a specific task [22]. Shock-induced failure of brittle components and electrical equipment (such as relays, switches, and glass diodes) has been reported in the literature [23]. Predicting pyrotechnic shock is indeed difficult because of the complex solid mechanics involved. However, because the valve's housing is stiff compared with the gas, its deformation, which is driven by the gas dynamics, only minimally affects the gas volume; thus, it is reasonable to assume that the gas dynamics are independent of the solid mechanics. In this respect, our gas-dynamic analysis can also provide leading-order information about pyrotechnic shock.

Specific objectives of this study are to characterize the 1) influence of gas-dynamic waves on both explosive burn and piston motion within axis-symmetric valves, 2) leading-order pyrotechnic shock produced during operation, and 3) influence of valve geometry and explosive mass on performance. Additionally, because of recent interests in miniaturization of explosively actuated devices, we examine how valve performance varies with reduction in size.

An outline of this paper is as follows. The unsteady quasi-1-D model (with assumptions, governing equations, initial conditions, and boundary conditions) is first posed in Sec. II. In Sec. III, the initial boundary-value problem (IBVP) describing valve operation is expressed in terms of generalized coordinates to facilitate its numerical integration, the numerical integration strategy is discussed, and simple problems with analytical solutions are simulated for model verification. In Sec. IV, baseline valve predictions are presented and compared with experimental data. An analysis is performed in Sec. V to characterize the sensitivity of predictions to parameters of design importance, as well as those associated with the constitutive theory, and miniature valve predictions are presented and discussed in Sec. VI. Finally, conclusions and recommendations for future work are summarized in Sec. VII.

II. Model Description

The mathematical model is formulated in this section. The model describes 1) pressure-dependent burn of a granular solid explosive, 2) mass and acoustic energy transport within and between the actuator and expansion chamber, and 3) piston motion within the valve bore driven by high-pressure gas acting on its surface and opposed by piston-housing interference.

Figure 2 depicts the simplified axisymmetric valve modeled in this study. Important geometrical features of the actual valve are retained, including cross-sectional area variations with axial position, volume changes within the actuator due to explosive burn, and volume changes within the expansion chamber due to piston motion. The quasi-1-D assumption is reasonable for small continuous changes in cross-sectional area; as such, the abrupt area change near the port is considered to be smooth for this analysis. The small area variations occurring within the tapered region of the piston and expansion chamber [which are greatly exaggerated in Fig. 1a, for clarity] are

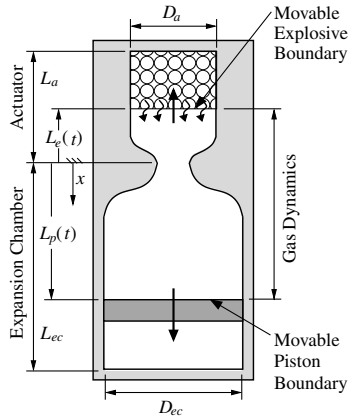

Fig. 2 Schematic of the simplified nitrogen cartridge valve with key model features.

ignored because they minimally affect the gas dynamics; consequently, the expansion chamber is modeled as having constant cross-sectional area beyond the port region. This slightly tapered region, however, does affect piston resistance, due to geometrical interference between the piston and valve bore. This interference is accounted for by the model, because it significantly affects piston motion and performance. Other simplifications and assumptions are explained later in this section. In Fig. 2, combustion product gas is confined to the domain $-L_e(t) \le x \le L_p(t)$, where $L_e(t)$ and $L_p(t)$ are the instantaneous locations of the explosive and piston boundaries, respectively. Gas mass, momentum, and energy fluxes due to combustion are imposed at $L_e(t)$, and an equation of motion for the piston is imposed at $L_p(t)$. An increase in gas volume within the valve results from the axial motion of these boundaries with time.

A. Equations

Equations governing the evolution of combustion product-gas mass, momentum, and energy within the domain $-L_e(t) < x < L_p(t)$ are classical and are given by the quasi-1-D equations [24], respectively,

$$\frac{\partial}{\partial t}(A\rho) + \frac{\partial}{\partial x}(A\rho u) = 0 \tag{1}$$

$$\frac{\partial}{\partial t}(A\rho u) + \frac{\partial}{\partial x}[A(\rho u^2 + p)] = p\,\frac{\mathrm{d}A}{\mathrm{d}x} \tag{2}$$

$$\frac{\partial}{\partial t}(A\rho E) + \frac{\partial}{\partial x}\left[A\rho u\left(E + \frac{p}{\rho}\right)\right] = 0 \tag{3}$$

Independent variables appearing in these equations include time t and axial position x. Dependent variables include gas density ρ, velocity u, pressure p, and total specific energy $E = e + u^2/2$, where e is mass specific internal energy. The forcing term in Eq. (2) represents an axial momentum exchange with the surroundings induced by pressure interactions along the curved surface of the valve wall. Because of the valve's fast operation time, heat transfer to the surroundings is small and is ignored. The axial variation in valve cross-sectional area $A(x)$ is a prescribed function that is representative of the actual valve geometry. Moving area terms to the right of the equalities in Eqs. (1–3) gives

$$\frac{\partial}{\partial t}(\rho) + \frac{\partial}{\partial x}(\rho u) = -\rho u\,\frac{1}{A}\,\frac{\mathrm{d}A}{\mathrm{d}x} \tag{4}$$

$$\frac{\partial}{\partial t}(\rho u) + \frac{\partial}{\partial x}(\rho u^2 + p) = -\rho u^2\,\frac{1}{A}\,\frac{\mathrm{d}A}{\mathrm{d}x} \tag{5}$$

$$\frac{\partial}{\partial t}(\rho E) + \frac{\partial}{\partial x}\left[\rho u\left(E + \frac{p}{\rho}\right)\right] = -\rho u\left(E + \frac{p}{\rho}\right)\frac{1}{A}\,\frac{\mathrm{d}A}{\mathrm{d}x} \tag{6}$$

This form of the governing equations is preferred in this study, because $A(x)$ is prescribed and the derivative $\mathrm{d}A/\mathrm{d}x$ can be directly evaluated. Thermal and caloric equations of state for the gas are assumed to be ideal and are given, respectively, by

$$p = \rho RT, \qquad e = c_v T \tag{7}$$

where R is the gas constant and c_v is the constant volume specific heat. Values for R and c_v were chosen to match values for HMX product compositions [25] predicted by the CHEMKIN thermochemistry package.

Equations (4–7) constitute a system of five equations and five unknowns (i.e., ρ, u, e, p, and T). Initial conditions prescribed on the domain $L_e^0 \le x \le L_p^0$, where L_e^0 and L_p^0 are the initial boundary locations, and are given by

$$p(x,0) = p^0, \qquad T(x,0) = T^0, \qquad u(x,0) = 0 \tag{8}$$

The gas equations of state are used to evaluate $\rho^0 = \rho(p^0, T^0)$ and $e^0 = e(T^0)$. Appropriate boundary conditions are specified in the following subsections.

B. Boundary Conditions

Product-gas mass, momentum, and energy fluxes imposed at $x = -L_e(t)$ are determined based on a simple combustion model. To this end, it is assumed that the ignition process, triggered by an embedded hot wire in practice, occurs quickly and uniformly throughout the explosive, producing N_e simultaneously burning spherical grains within the combustion zone depicted in Fig. 3a. It is further assumed that the combustion zone is well-stirred so that no spatial variations in explosive and gas properties exist within it. Ignoring kinetic energy changes, the evolution of mass and energy for the solid explosive and product gas contained within the combustion zone are described by

$$\frac{\mathrm{d}}{\mathrm{d}t}(\rho_e \phi_e V_c) = -\rho_e A_e r_e \tag{9}$$

$$\frac{\mathrm{d}}{\mathrm{d}t}(\rho_g \phi_g V_c) = \rho_e A_e r_e - \dot{m}_g \tag{10}$$

$$\frac{\mathrm{d}}{\mathrm{d}t}(\rho_e \phi_e V_c e_e) = -\rho_e A_e r_e e_e \tag{11}$$

$$\frac{\mathrm{d}}{\mathrm{d}t}(\rho_g \phi_g V_c e_g) = \rho_e A_e r_e e_e - \dot{m}_g\left(e + \frac{p}{\rho} + \frac{u^2}{2}\right) \tag{12}$$

where explosive properties are denoted by subscript e, and gas properties contained within the combustion zone are denoted by subscript g. Forcing terms in Eqs. (9–12) account for mass and energy exchange between the explosive and gas, due to combustion and flow of gas mass and energy through the explosive boundary into the remaining actuator volume, as depicted in Fig. 3b. Note that all explosive mass is confined to the combustion zone within the context

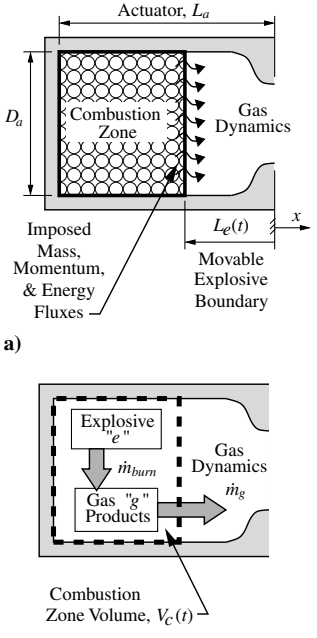

Fig. 3 Schematic of the explosive boundary and combustion zone: a) hypothetical schematic used for model development and b) representation of thermodynamic interactions.

of this model. New variables appearing in these equations include the explosive and gas volume fractions $\phi_e = V_e/V_c$ and $\phi_g = V_g/V_c$, the combustion zone volume V_c, the explosive-burn rate r_e, the explosive-burn surface area A_e, and the product-gas mass flow rate through the explosive boundary $\dot{m}_g$, where $\dot{m}_g = \rho u A_a$, and A_a is the actuator cross-sectional area. From mixture theory, the explosive and gas products within the combustion zone are constrained by the condition

$$\phi_e + \phi_g = 1 \tag{13}$$

The combustion zone volume decreases with time as the explosive burns and gas products flow across the explosive boundary. The time-dependent combustion zone volume is given by

$$V_c(t) = A_a(L_a - L_e(t)) \tag{14}$$

where L_a is the constant actuator length. As commonly done, the explosive-burn rate is taken to be pressure-dependent [26]. Expressions for the explosive-burn rate, radius of a single burning grain, and total explosive-burn surface area are given by

$$r_e \equiv -\frac{\mathrm{d}R_e}{\mathrm{d}t} = ap^n, \qquad R_e = \left(\frac{3\phi_e V_c}{4\pi N_e}\right)^{1/3}, \qquad A_e = 4\pi R_e^2 N_e \tag{15}$$

where a and n are empirically determined burn-rate constants. The explosive is assumed to be incompressible (i.e., $\rho_e = \rho_e^0$), and heat interaction between the explosive and product gas is ignored. As such, it can be shown by multiplying Eq. (9) by e_e and subtracting the result from Eq. (11) that the explosive specific internal energy is constant during combustion (i.e., $e_e = e_e^0$).

For simplicity, it is assumed that $\phi_g \ll 1$ within the combustion zone. Therefore, to leading order, $\phi_g \approx 0$ and $\phi_e = 1 - \phi_g \approx 1$ from Eq. (13). Substituting $\phi_e = 1$ and the geometrical relation for V_c into Eq. (9) and rearranging the result gives

$$\frac{\mathrm{d}L_e}{\mathrm{d}t} = \frac{A_e}{A_a} r_e \tag{16}$$

which describes the evolution of the explosive boundary; the initial condition for this equation is $L_e(0) = L_e^0$. In this limit ($\phi_e \approx 1$), the last two expressions in Eq. (15) reduce to

$$R_e(t) = \left[\frac{3A_a(L_a - L_e(t))}{4\pi N_e}\right]^{1/3}, \qquad A_e(t) = 4\pi R_e(t)^2 N_e \tag{17}$$

Note that Eq. (16) depends on the gas pressure at the explosive boundary through $r_e(p)$; this pressure is numerically estimated based on a linear extrapolation of pressure from within the gas domain, as explained in the following section. Consequently, gas-pressure waves occurring within the actuator chamber will influence explosive combustion. Likewise, substituting $\phi_g = 0$ into Eqs. (10) and (12) and rearranging the resulting algebraic expressions gives gas mass and energy fluxes at the explosive boundary:

$$\rho u = \frac{\dot{m}_g}{A_a} = \frac{\rho_e^0 A_e r_e}{A_a} \tag{18}$$

$$\rho u\left(e + \frac{p}{\rho} + \frac{u^2}{2}\right) = \frac{\rho_e^0 A_e r_e q}{A_a} \tag{19}$$

where $q \equiv e_e^0$ is the specific combustion energy of the explosive. Equations (18) and (19) contain the four unknowns ρ, u, e, and p. Given the product-gas pressure at the explosive boundary p and using the gas equations of state, then Eqs. (18) and (19) can be combined to obtain a quadratic expression for ρ:

$$\rho^2 - \frac{p}{q}\left(\frac{\gamma}{\gamma - 1}\right)\rho - \frac{1}{2q}\left(\frac{\rho_e^0 A_e r_e}{A_a}\right)^2 = 0$$

Numerical experiments indicate that only one root of this expression is nonnegative and thus physically meaningful. Corresponding values for $u(\rho, p)$ and $e(\rho, p)$ can be obtained from Eqs. (18) and (19). The product-gas momentum flux at the explosive boundary is then specified by $\rho u(\rho, p)^2 + p$. Once combustion is complete at $t = t_{\mathrm{burn}}$, then $L_e(t) = L_a$, and the boundary condition is switched to a zero-mass-flux condition, which requires that $u(L_a, t) \equiv 0$ for $t \geq t_{\mathrm{burn}}$.

We now specify the piston boundary condition imposed at $x = L_p(t)$. Newton's law of motion for the piston is given by

$$m_p \frac{\mathrm{d}^2}{\mathrm{d}t^2}(L_p) = F_p - F_R \tag{20}$$

where $L_p(t)$ is the piston axial location, m_p is the piston mass, F_p is the gas-dynamic pressure force, and F_R is the piston-bore resistance force. As mentioned, cross-sectional-area variations associated with the hollow piston are ignored because they are small, and the piston is modeled as a flat disc within the context of our gas-dynamic model. The gas-dynamic pressure force acting on the piston is given by

$$F_p(t) = p(L_p(t), t)A_p \tag{21}$$

where $A_p = \pi D_{\mathrm{ec}}^2/4$ is the constant piston cross-sectional area. The initially tapered piston skirt and its thickness are important, however, in determining the piston-bore resistance force. We account for this force using the elastic–plastic piston-housing deformation model developed by Braud et al. [20]. Here, we only discuss key features of this model, as the cited references gives a comprehensive derivation and discussion.

The piston resistance model is based on cylindrical-pressure-vessel theory. The resistance force is determined by the interface stress between the piston and housing, which depends on their material properties and thicknesses. The piston skirt is assumed to initially lie completely within the shallow tapered region of the expansion chamber located immediately adjacent to the valve bore. Only the skirt contributes to piston resistance; the remaining part of the piston that initially resides within the bore is assumed to be frictionless.

The skirt gradually deforms as it is pushed into the bore by gas pressure, as illustrated in Fig. 4a. The resistance force consists of two components:

$$F_R(t) = F_{\mathrm{skirt}}(t) + F_{\mathrm{bore}}(t) \tag{22}$$

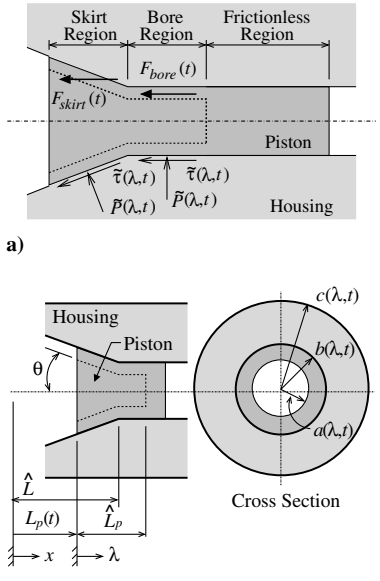

Fig. 4 Schematic of a) the piston regions and b) the coordinate system used by the piston resistance model.

where $F_{\text{skirt}}(t)$ accounts for that part of the skirt that instantaneously resides within the tapered section of the expansion chamber, referred to as the skirt region, and $F_{\text{bore}}(t)$ accounts for the part of the skirt that has been pushed into the bore. Initially, $F_{\text{skirt}} = F_{\text{bore}} = 0$, and $F_{\text{skirt}} \to 0$ as the entire piston is pushed into the bore. During this process, geometrical interference and gas pressure cause a compressive radial stress to act along the skirt-housing interface (i.e., $\sigma_r = -\tilde{P}$); the gas pressure is taken to be the instantaneous pressure acting at the piston boundary $p(L_p(t), t)$. The interface stress locally induces a tangential traction given by $\tilde{\tau} = -\mu\tilde{P}$, where μ is a constant friction coefficient. Because the interference will generally vary with both axial position and time, then $\tilde{P} = \tilde{P}(\lambda, t)$ and $\tilde{\tau} = \tilde{\tau}(\lambda, t)$, where λ is an axial coordinate measured relative to the top of the piston, as illustrated in Fig. 4b. The inner, interface, and outer radii of the skirt-housing cross section at a given axial location are denoted by $a(\lambda, t)$, $b(\lambda, t)$, and $c(\lambda, t)$, respectively. The resistive force components are therefore given by

$$F_{\text{skirt}}(t) = (\mu_s \cos\theta + \sin\theta) \int_{A_{\text{skirt}}} \tilde{P}(\lambda, t)\, \mathrm{d}A$$
$$F_{\text{bore}}(t) = \mu_b \int_{A_{\text{bore}}} \tilde{P}(\lambda, t)\, \mathrm{d}A \tag{23}$$

where μ_s and μ_b are the friction coefficients in the skirt and bore regions, and θ is the initial skirt taper angle measured relative to the axis of symmetry. The friction-coefficient values were determined by quasi-static compression tests performed on actual nitrogen cartridge valves [20]. Because the skirt and bore regions have the shape of a conical frustum and cylinder, respectively, the integrals in Eq. (23) can be reduced to one-dimensional integrals in terms of λ:

$$F_{\text{skirt}}(t) = (\mu_s \cos\theta + \sin\theta) \int_0^{\hat{L}-L_p(t)} \tilde{P}(\lambda, t) g(\lambda, t)\, \mathrm{d}\lambda$$
$$F_{\text{bore}}(t) = 2\pi\mu_b R_b \int_{\hat{L}-L_p(t)}^{\hat{L}_p} \tilde{P}(\lambda, t)\, \mathrm{d}\lambda \tag{24}$$

where

$$g(\lambda, t) = \pi\sqrt{[b(0,t) - b(\lambda,t)]^2 + \lambda^2} \times \left[\frac{\partial b}{\partial \lambda} + \frac{[b(0,t) + b(\lambda,t)](\lambda - [b(0,t) - b(\lambda,t)]\frac{\partial b}{\partial \lambda})}{[b(0,t) - b(\lambda,t)]^2 + \lambda^2}\right]$$

and

$$b(\lambda, t) = \left[\frac{R_b - b(0,t)}{\hat{L} - L_p(t)}\right]\lambda + b(0,t)$$

The constant bore radius is given by R_b.

It is further assumed that the piston and housing experience only small deformations. Thus, the piston length $\hat{L}_p$ remains approximately constant, since θ is small ($\approx 9°$). To complete the evaluation of $F_R(t)$, the interface stress $\tilde{P}(\lambda, t)$ must be estimated. This stress is locally evaluated based on a steady, two-dimensional, elastic–plastic plane-strain theory, which assumes that the stress field rapidly equilibrates during piston motion. This equilibrium assumption is reasonable, because the acoustic speeds within the piston and housing are significantly larger than that of the high-temperature product gas. Details of the derivation and solution behavior are given in [20].

Using the expressions for F_p and F_R, Eq. (20) can be numerically integrated to determine piston position and velocity. To this end, the second-order ODE is split into an equivalent first-order system:

$$m_p \frac{\mathrm{d}v_p}{\mathrm{d}t} = F_p - F_R \tag{25}$$

$$\frac{\mathrm{d}L_p}{\mathrm{d}t} = v_p \tag{26}$$

where $v_p(t)$ is the piston velocity. Initial conditions for these equations are $v_p(0) = 0$ and $L_p(0) = L_p^0$. A zero-mass-flux condition is imposed on the product gas at the piston boundary, which requires that $u(L_p(t), t) = v_p(t)$. Once the piston completes its stroke at $t = t_{\text{stk}}$, then $L_p(t) = L_{\text{ec}}$ and $u(L_{\text{ec}}, t) = 0$ for $t \geq t_{\text{stk}}$.

In summary, the IBVP is given by Eqs. (4–7), with the initial conditions of Eq. (8), and the stated boundary conditions at $L_e(t)$ and $L_p(t)$.

C. Pyrotechnic Shock

The time-dependent axial force transmitted to the valve's supporting structure is given by

$$F_{\text{pyro}}(t) = F_a(t) + F_{p,a}(t) + F_{\text{ec}}(t) \tag{27}$$

where $F_a(t)$ is the pressure force that acts on the rear planar actuator surface, $F_{p,a}(t)$ is the net axial pressure force that acts on the curved surfaces of the valve, and $F_{\text{ec}}(t)$ is the transmitted force that acts on the housing through piston contact. For the purposes of this study, this force is interpreted as the pyrotechnic shock, even though it does not directly account for the rate-dependent dissipation that is likely to occur within structural components.

The pressure force $F_a(t)$ that acts on the planar actuator surface at $x = -L_a$ is based on the local stagnation pressure, because the velocity is zero at that location:

$$F_a(t) = -p_0(t) A_a \tag{28}$$

where the stagnation pressure p_0 is given by

$$p_0(t) = p(-L_e(t), t)\left[1 + \frac{\gamma - 1}{2} Ma(-L_e(t), t)^2\right]^{\frac{\gamma}{\gamma-1}} \tag{29}$$

Here, $Ma(-L_e(t), t)$ is the Mach number at the explosive boundary, and γ is the specific heat ratio. Once combustion is complete, then $Ma(-L_a, t) = 0$ so that $p_0(t) = p(-L_a, t)$. The net axial pressure force $F_{p,a}(t)$ that acts on the curved surface is obtained by integration; given the spatial variation in valve diameter $D(x)$, the following expression is obtained:

$$F_{p,a}(t) = -\frac{\pi}{2} \int_{L_e(t)}^{L_p(t)} p(x, t) D(x) \frac{\mathrm{d}D}{\mathrm{d}x}\, \mathrm{d}x \tag{30}$$

Depending on the pressure fields within the actuator and expansion chamber, this force may act in either direction. As the piston is inserted into the bore, it exerts a reaction force $F_{\text{ec}}(t)$ on the valve housing that acts in the positive x direction. Following piston stroke, the piston comes to rest and the pressure force is entirely transmitted to the housing. Therefore, $F_{\text{ec}}(t)$ is given by

$$F_{\text{ec}}(t) = \begin{cases} F_R(t) & \text{for } t < t_{\text{stk}} \\ p(L_{\text{ec}}, t) A_p & \text{for } t \geq t_{\text{stk}} \end{cases} \tag{31}$$

III. Numerics

The method used to integrate the IBVP posed in the previous section is now described. The governing equations are first expressed in terms of generalized coordinates to facilitate their numerical integration on the expanding domain $L_e(t) \leq x \leq L_p(t)$, subject to flux conditions at the explosive and piston boundaries. The technique used to numerically solve the transformed equations is then briefly described, followed by representative predictions that establish both numerical verification and convergence.

A. Generalized Coordinates

Equations (4–6) are expressed in terms of generalized coordinates on a fixed computational domain using the algebraic transformation

$$\xi = \frac{x - L_e(t)}{L_p(t) - L_e(t)}, \qquad \tau = t$$

where $\xi \in [0, 1]$ and $\tau \in [0, \infty)$, respectively. The differential operators are determined by direct application of the chain rule:

$$\left.\frac{\partial}{\partial x}\right|_t = \xi_x|_t \left.\frac{\partial}{\partial \xi}\right|_\tau, \qquad \left.\frac{\partial}{\partial t}\right|_x = \xi_t|_x \left.\frac{\partial}{\partial \xi}\right|_\tau + \left.\frac{\partial}{\partial \tau}\right|_\xi \tag{32}$$

where the grid metrics are given by $\xi_x = 1/x_\xi$ and $\xi_t = -x_\tau/x_\xi$. The metric ξ_x is the Jacobian, which accounts for grid stretching. These metrics can either be evaluated by direct differentiation or by finite differencing using grid-point locations in both coordinate systems. In this work, the metrics are evaluated by finite differencing to generalize our algorithm for future inclusion of more complex transformations. Simulations were conducted with the grid metrics evaluated by both methods, and the results were indifferent.

Applying the differential operators given by Eq. (32) to Eqs. (4–6) and rearranging the results gives the following equations expressed in terms of generalized coordinates:

$$\frac{\partial}{\partial \tau}\left(\frac{\rho}{\xi_x}\right) + \frac{\partial}{\partial \xi}\left(\frac{\rho U^c}{\xi_x}\right) = -\rho u \frac{1}{A}\frac{\partial A}{\partial \xi} \tag{33}$$

$$\frac{\partial}{\partial \tau}\left(\frac{\rho u}{\xi_x}\right) + \frac{\partial}{\partial \xi}\left[\frac{1}{\xi_x}(\rho u U^c + \xi_x p)\right] = -\rho u^2 \frac{1}{A}\frac{\partial A}{\partial \xi} \tag{34}$$

$$\frac{\partial}{\partial \tau}\left(\frac{\rho E}{\xi_x}\right) + \frac{\partial}{\partial \xi}\left[\frac{\rho}{\xi_x}\left(E U^c + u\frac{\xi_x p}{\rho}\right)\right] = -\rho u\left(E + \frac{p}{\rho}\right)\frac{1}{A}\frac{\partial A}{\partial \xi} \tag{35}$$

The variable U^c appearing in these equations is the contravariant velocity defined by $U^c = \xi_t + \xi_x u$, which is the velocity of the gas in the ξ direction. Equations (33–35) constitute a strictly hyperbolic system of partial differential equations; the eigenvalues of the generalized flux Jacobian matrix ($\partial \mathbf{f}/\partial \mathbf{q}$, where $\mathbf{f}$ and $\mathbf{q}$ are defined in the following subsection) are both real and distinct and are given by U^c, $U^c + \xi_x c$, and $U^c - \xi_x c$, where $c = \sqrt{\gamma RT}$ is the sound speed. These eigenvalues are needed for the implementation of the numerical technique. A complete derivation of the transformed equations and the eigenvalues of the generalized flux Jacobian matrix can be found in [25].

The boundary conditions established in the preceding section are expressed in terms of generalized coordinates by applying Eq. (32) to Eq. (16) for the explosive boundary and to Eqs. (25) and (26) for the piston boundary; the resulting expressions are given by

$$\frac{dL_e}{d\tau} = \frac{A_e}{A_a} r_e \tag{36}$$

$$m_p \frac{dv_p}{d\tau} = F_p - F_R \tag{37}$$

$$\frac{dL_p}{d\tau} = v_p \tag{38}$$

Equation (36) is imposed at $\xi = 0$, and Eqs. (37) and (38) are imposed at $\xi = 1$. Since $L_e(t)$, $v_p(t)$, and $L_p(t)$ are functions of time only, Eqs. (36–38) are identical to those expressed in the physical domain.

B. Kurganov–Tadmor Technique

The high-resolution numerical technique used in this study to integrate the model equations was formulated by Kurganov and Tadmor [27]. This technique is total variation diminishing (TVD), enabling shocks to be resolved with minimal artificial diffusion and dispersion. Only the eigenvalues of the flux Jacobian matrix are used; no additional knowledge of the model eigenstructure is required. To implement this technique, it is necessary to express Eqs. (33–35) in the vector conservative form:

$$\frac{\partial}{\partial \tau}\mathbf{q}(\xi, \tau) + \frac{\partial}{\partial \xi}\mathbf{f}(\mathbf{q}(\xi, \tau)) = \mathbf{w}(\mathbf{q}(\xi, \tau)) \tag{39}$$

where $\mathbf{q} \in \Re^3$ is the conserved variable vector, $\mathbf{f}(\mathbf{q}) \in \Re^3$ is the flux vector, and $\mathbf{w}(\mathbf{q}) \in \Re^3$ is the source vector ($\Re^3$ is a set of three real numbers):

$$\mathbf{q} = \left[\frac{\rho}{\xi_x}, \frac{\rho u}{\xi_x}, \frac{\rho E}{\xi_x}\right]^T$$

$$\mathbf{f}(\mathbf{q}) = \left[\frac{\rho U^c}{\xi_x}, \frac{1}{\xi_x}(\rho u U^c + \xi_x p), \frac{\rho}{\xi_x}\left(E U^c + u\frac{\xi_x p}{\rho}\right)\right]^T$$

$$\mathbf{w}(\mathbf{q}) = \left[-\rho u \frac{1}{A}\frac{\partial A}{\partial \xi}, -\rho u^2 \frac{1}{A}\frac{\partial A}{\partial \xi}, -\rho u\left(E + \frac{p}{\rho}\right)\frac{1}{A}\frac{\partial A}{\partial \xi}\right]^T$$

A semidiscrete finite volume form of Eq. (39) is numerically integrated on a fixed domain that is discretized into N_ξ evenly spaced cells of width $\Delta\xi = 1/N_\xi$. Cell centers are located at positions ξ_j ($j = 1, \ldots, N_\xi$), and corresponding cell interfaces are located at positions $\xi_{j\pm 1/2} = \xi_j \pm \Delta\xi$. The semidiscrete system of ODEs is given by

$$\frac{d\mathbf{Q}_j(\tau)}{d\tau} = -\frac{\mathbf{F}_{j+1/2}(\tau) - \mathbf{F}_{j-1/2}(\tau)}{\Delta\xi} + \mathbf{W}_j(\tau), \tag{40}$$

where $\mathbf{Q}_j(\tau)$ is a numerical approximation to $\mathbf{q}(\xi_j, \tau)$, $\mathbf{F}_{j+1/2}(\tau)$ and $\mathbf{F}_{j-1/2}(\tau)$ are numerical flux vectors, and $\mathbf{W}_j(\tau)$ is a numerical approximation to $\mathbf{w}(\xi_j, \tau)$. The numerical flux function is defined by:

$$\mathbf{F}_{j+1/2}(\tau) = \frac{\mathbf{f}(\mathbf{q}^+_{j+1/2}(\tau)) + \mathbf{f}(\mathbf{q}^-_{j+1/2}(\tau))}{2} - \frac{c_{j+1/2}(\tau)}{2}[\mathbf{q}^+_{j+1/2}(\tau) - \mathbf{q}^-_{j+1/2}(\tau)] \tag{41}$$

where $c_{j+1/2}$ is the maximum eigenvalue wave speed based on the extrapolated values $\mathbf{q}^\pm_{j+1/2}$, which are defined by

$$\mathbf{q}^+_{j+1/2}(\tau) \equiv \mathbf{Q}_{j+1}(\tau) - \frac{\Delta\xi}{2}(\partial\mathbf{q}/\partial\xi)_{j+1}(\tau)$$
$$\mathbf{q}^-_{j+1/2}(\tau) \equiv \mathbf{Q}_j(\tau) + \frac{\Delta\xi}{2}(\partial\mathbf{q}/\partial\xi)_j(\tau) \tag{42}$$

Equation (40) is numerically integrated in time using an explicit fourth-order-accurate Runge–Kutta (4RK) technique. The integration time step $\Delta\tau$ is chosen based on a Courant–Friedrichs–Lewy (CFL) condition for numerical stability (a CFL number of 0.4 was used for all simulations performed in this study). Boundary conditions given by Eqs. (36–38) are also simultaneously integrated in time using the 4RK technique. The numerical algorithm is nominally second-order-accurate in space and fourth-order-accurate in time.

The Kurganov–Tadmor technique requires that the spatial derivatives $\partial\mathbf{q}/\partial\xi$ in Eq. (42) be computed on the computational grid in a manner that preserves the TVD property. These derivatives are estimated from cell averages using a ϑ-dependent minmod limiter:

$$\left.\frac{\partial \mathbf{q}}{\partial \xi}\right|_j \approx \text{minmod}\left(\vartheta\frac{\mathbf{Q}_j - \mathbf{Q}_{j-1}}{\Delta\xi}, \frac{\mathbf{Q}_{j+1} - \mathbf{Q}_{j-1}}{2\Delta\xi}, \vartheta\frac{\mathbf{Q}_{j+1} - \mathbf{Q}_j}{\Delta\xi}\right) \tag{43}$$

where the minmod function is defined by

$$\text{minmod}\,(d_1, d_2, d_3) = \begin{cases} \min(d_i), & \text{if } d_i > 0 \;\forall\; i \\ \max(d_i), & \text{if } d_i < 0 \;\forall\; i \\ 0, & \text{otherwise} \end{cases} \tag{44}$$

The numerical parameter $\vartheta \in [1, 2]$ is selected in a manner that optimizes resolution of discontinuities.

C. Verification and Convergence

Three problems with analytical solutions were simulated to verify our implementation of the numerical technique: 1) steady flow through a Laval nozzle, 2) a shock-tube problem, and 3) unsteady expansion induced by two impulsively retracted pistons. Each problem represents a limiting-form solution of the governing equations. The first problem was chosen to verify effects of area variation on time-independent grids, the second problem was chosen to verify the coupled space–time accuracy of the technique, and the third problem was chosen to verify grid metrics for an expanding computational domain. A comprehensive discussion of all verification problems is given in [25].

Steady isentropic gas flow through a Laval (converging–diverging) nozzle is addressed. For this analysis, subsonic upstream flow within the converging section of the nozzle was imposed, with subsonic and supersonic flow within the diverging section separately considered. Analytical solutions to this problem are classical [28]. Equations (33–35), with $\xi_x = 1$ and $\xi_t = 0$, were numerically solved on the domain $0 \le \xi = x \le 1$, and nonreflecting conditions were imposed at both the upstream and downstream boundaries. The initial condition consisted of a motionless gas with a uniform high-pressure region to the left of the nozzle throat (located at $x = 0.5$ m) and a uniform lower-pressure region to the right. The prescribed nozzle cross-sectional area was $A(x) = \pi D(x)^2/4$, where

$$D(x) = \begin{cases} D_l & \text{for } x \le 0.25 \text{ m} \\ (D_l + D_t)/2 - (D_l - D_t)\cos(4\pi x)/2 & \text{for } 0.25 \le x \le 0.50 \text{ m} \\ (D_r + D_t)/2 - (D_r - D_t)\cos(4\pi x)/2 & \text{for } 0.50 \le x \le 0.75 \text{ m} \\ D_r & \text{for } x \ge 0.75 \text{ m} \end{cases} \tag{45}$$

Table 1 Parameter values and initial conditions used for the Laval nozzle problem

Subsonic Case			Supersonic case		
Parameter or initial condition	Value	Units	Parameter or initial condition	Value	Units
D_l	2.0	m	D_l	2.0	m
D_r	1.6	m	D_r	1.6	m
D_t	0.8	m	D_t	0.8	m
N_ξ	400	——	N_ξ	400	——
p_l^0	0.135	MPa	p_l^0	10.0	MPa
p_r^0	0.1	MPa	p_r^0	0.1	MPa
R	287.0	J/(kg · K)	R	287.0	J/(kg · K)
T_l^0	300.0	K	T_l^0	300.0	K
T_r^0	300.0	K	T_r^0	300.0	K
u_l^0	0.0	m/s	u_l^0	0.0	m/s
u_r^0	0.0	m/s	u_r^0	0.0	m/s
γ	1.4	——	γ	1.4	——
ϑ	1.5	——	ϑ	1.5	——

The subscripts l and r denote the maximum diameter to the left and right of the throat; the throat diameter is D_t. All parameters and initial conditions used in these simulations are listed in Table 1. Simulations were terminated once the flows reached steady state.

A comparison of the predicted and analytical solutions is given in Fig. 5; in this figure, the nozzle radius is highlighted by the dashed line. Figure 5a gives the steady Mach number profiles for both the subsonic and supersonic cases. Figures 5b and 5c give the pressure, density, and temperature ratios for the subsonic and supersonic cases, respectively, where the stagnation properties are given by the corresponding initial values in the converging section. The numerical and analytical solutions agree well in all cases.

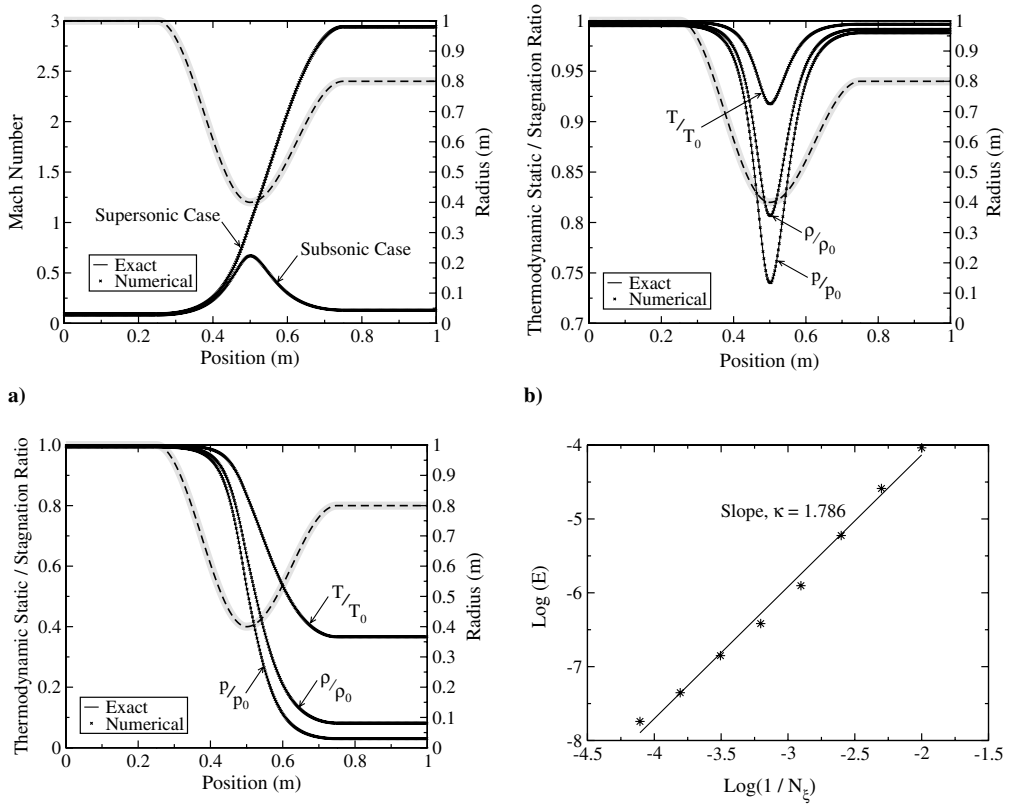

Fig. 5 Comparison of the analytical and numerical solutions for the Laval nozzle problem: a) Mach number, b) property ratios for the subsonic case, and c) property ratios for the supersonic case. The convergence-rate plot is shown in d).

To establish convergence of the technique, we define the error at time t^n by (for steady flow through the Laval nozzle, we take $t^n \to \infty$)

$$E(t^n) = \frac{1}{N_\xi} \sum_{j=1}^{N_\xi} \frac{|p(x_j, t^n) - \hat{p}(x_j, t^n)|}{p^r} \tag{46}$$

where $p(x_j, t^n)$ is the predicted pressure at position $x = x_j$, and $\hat{p}(x_j, t^n)$ is the corresponding analytical value. The quantity p^r is a reference pressure used to nondimensionalize the error. Assuming that $E \propto \Delta x^\kappa$ and that $\Delta x \propto 1/N_\xi$, where κ is the convergence rate, we have that

$$\log(E) \propto \kappa \log\left(\frac{1}{N_\xi}\right) \tag{47}$$

Thus, the convergence rate is given by the slope of a best-fit line in the $\log(E)$ vs $\log(1/N_\xi)$ plane. Figure 5d shows convergence-rate data for supersonic flow through the Laval nozzle for $100 \le N_\xi \le 12,800$ cells. The reference pressure was taken as $p^r = p_l^0$. These data indicate that $\kappa = 1.786$. High-resolution shock-capturing method slightly reduces its accuracy. Nonetheless, this convergence rate exceeds the value of $\kappa \approx 1$, which is typically computed for problems involving discontinuities such as shocks and contact waves, as shown subsequently.

Next, the 1-D shock-tube problem is considered, which involves the time-dependent breakup of an initial discontinuity that separates uniform regions of motionless gas with different thermodynamic states into self-similar waves consisting of a shock, contact discontinuity, and expansion; it represents a common benchmark problem for numerical techniques applied to hyperbolic conservation laws [29]. States to the left and right of the initial discontinuity are labeled with l and r subscripts. This problem is governed by Eqs. (33–35), with $\partial A/\partial x = 0$, $\xi_x = 1$, and $\xi_t = 0$. The initial discontinuity is located at $x = 0.5$ m on the domain $0 \le x = \xi \le 1$ m. The domain is chosen to be sufficiently long so that waves do not encounter the boundaries during the simulation; thus, boundary conditions need not be imposed. All parameters and initial conditions used for this simulation are listed in Table 2. A comparison between the analytical and predicted pressure at $t = 0.6$ ms is shown in Fig. 6a; arrows in the plots indicate wave-propagation directions. Because this solution is classical, it is not discussed in detail here (details can be found in [29]). Overall, agreement is good, with the shock captured within three–four computational cells. Figure 6b shows convergence-rate data for the shock-tube problem for $100 \le N_\xi \le 12,800$ cells. The reference pressure was taken as $p^r = p_l^0$. These data indicate that $\kappa = 1.014$. Though a value of $\kappa \approx 2$ might be anticipated, high-resolution shock-capturing methods reduce to near-first-order accuracy in the vicinity of discontinuities, due to artificial viscosity.

Table 2 Parameter values and initial conditions used for the classical shock-tube problem

Parameter or initial condition	Value	Units
N_ξ	400	——
p_l^0	1.0	MPa
p_r^0	0.1	MPa
R	287.0	J/(kg · K)
T_l^0	300.0	K
T_r^0	250.0	K
u_l^0	0.0	m/s
u_r^0	0.0	m/s
γ	1.4	——
ϑ	1.25	——

Finally, we verify our implementation of the grid metrics for a physical domain that expands with time due to impulsively retracted, constant-velocity pistons at its boundaries. The pistons bound an initially motionless gas with uniform properties. A centered expansion wave emanates from each piston surface, propagating into the gas with time. A self-similar analytical solution exists for each wave, which is valid before they merge and nonlinearly interact [30]. This problem is governed by Eqs. (33–35), with $\partial A/\partial x = 0$. The generalized coordinate transformation is given by

$$\xi = \frac{x - x_{p,l}(t)}{x_{p,r}(t) - x_{p,l}(t)}$$

where subscript l and subscript r denote the left and right piston boundaries. The locations of these boundaries are given by $x_{p,l}(t) = x_{p,l}^0 + v_{p,l}t$ and $x_{p,r}(t) = x_{p,r}^0 + v_{p,r}t$, where $v_{p,l}$ and $v_{p,r}$ are their prescribed constant velocities, and $x_{p,l}(0) = x_{p,l}^0$ and $x_{p,r}(0) = x_{p,r}^0$ are their prescribed initial positions. A zero-mass-flux condition is imposed on the gas at each boundary, which requires that $u(x_{p,l}(t), t) = v_{p,l}$ and $u(x_{p,r}(t), t) = v_{p,r}$. Initial conditions and parameters used for this problem are listed in Table 3. A comparison of the numerically predicted and analytical pressure profiles is shown in Fig. 7a at $t = 1.00$, 1.75, and 2.50 ms; the left and right boundaries in these plots correspond to the piston locations at $t = 2.50$ ms, and the arrows indicate wave-propagation directions. Though a slight discrepancy exists in the vicinity of the expansion-wave edges due to artificial viscosity, the predicted and analytical solutions agree well; wave speeds, magnitudes, and growth rates are accurately predicted. Figure 7b shows convergence-rate data based on the solution at $t = 1.75$ ms for $100 \le N_\xi \le 12800$ cells. The initial pressure was used as the reference pressure in Eq. (46). The convergence rate was computed to be $\kappa = 1.004$, which is comparable with the value for the shock-tube problem, due to the existence of singularities in the first spatial derivative of the solution at the wave edges.

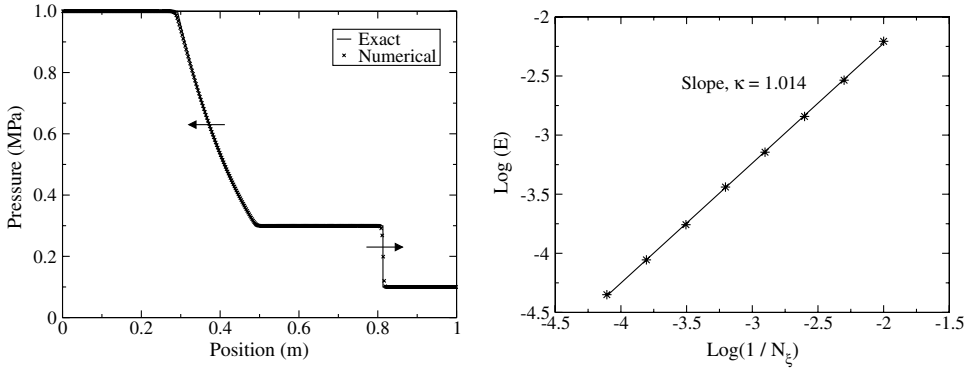

a) b)

Fig. 6 Comparison of analytical and predicted solutions for the shock-tube problem at $t = 0.6$ ms: a) pressure and b) convergence-rate data.

Table 3 Parameter values and initial conditions used for the retracting pistons problem

Parameter or initial condition	Value	Units
N_ξ	400	——
p^0	1.0	MPa
R	287.0	J/(kg · K)
T^0	300.0	K
u^0	0.0	m/s
$v_{p,l}$	−100.0	m/s
$v_{p,r}$	50.0	m/s
$x^0_{p,l}$	0.0	m
$x^0_{p,r}$	2.0	m
γ	1.4	——
ϑ	1.3	——

IV. Baseline Valve Predictions

Predictions are now given for a baseline valve configuration having dimensions that are representative of the conventional nitrogen cartridge valve depicted in Fig. 1. The prescribed cross-sectional area distribution is given by $A(x) = \pi D(x)^2/4$, where

$$D(x) = \begin{cases} D_a & \text{for } x \le -L^0_e \\ (D_a + D_t)/2 - (D_a - D_t)\cos(\pi x/L^0_e)/2 & \text{for } -L^0_e \le x \le 0 \\ (D_{\text{ec}} + D_t)/2 - (D_{\text{ec}} - D_t)\cos(2\pi x/L^0_p)/2 & \text{for } 0 \le x \le L^0_p/2 \\ D_{\text{ec}} & \text{for } x \ge L^0_p/2 \end{cases} \tag{48}$$

Values for the model parameters are listed in Table 4. All simulations were performed on a Linux workstation with an Intel Xeon 3.0 GHz processor with 4.6 GB of memory. A typical run time for a single simulation with $N_\xi = 2000$ cells is approximately 30 min. This value of N_ξ was used for all simulations, because numerical experiments indicate minimal variation in predicted stroke time for $N_\xi > 1000$ nodes [25].

Pressure-field predictions for the baseline configuration are shown in Fig. 8 at various times following ignition; horizontal arrows in the plots indicate the direction of wave propagation, and dashed lines indicate the axial variation in device radius. Only the gas region bounded by the explosive and piston boundaries is shown. Immediately following ignition at $t = 0$ μs, a product-gas shock emanates from the explosive boundary, driven by the production of gas mass, momentum, and energy, which strengthens as it propagates through the converging section of the device. This lead shock, as shown in Fig. 8a at $t = 0.38$ μs, is partly transmitted through the port and into the expansion chamber, causing the gas mass flow rate to choke at the port throat. Some acoustic energy is reflected back through the actuator, further increasing the combustion rate as it subsequently interacts with the explosive. Consequently, a secondary compression wave is formed near the explosive boundary that again propagates toward the port. As these shocks propagate through the diverging section of the expansion chamber, a compression wave develops behind the shocks, as shown in Fig. 8a at $t = 2.12$ μs. The subplot in Fig. 8a illustrates these waves at $t = 2.12$ μs across the spatial domain $1.0 \le x \le 3.0$ mm. The compression wave strengthens and becomes a third shock as it slowly follows the two leading shocks. The first two shocks coalesce, resulting in a single, stronger, lead shock and multiple weak rarefaction and contact waves. The new lead shock subsequently reflects off the piston surface and coalesces with the third shock, again resulting in a single, stronger, shock and multiple weak rarefaction and contact waves. Though complex wave interactions occur within the expansion chamber, the actuator pressure profiles remain smooth as combustion proceeds.

Figure 8b shows the pressure field at $t = 12.70$ μs, where a peak pressure of approximately 820 MPa is predicted within the actuator, and the remaining shock is observed at $x \approx 5.5$ mm. As the actuator depressurizes, gas flow remains choked at the port. During this period, pressure fields within the entire valve are mostly smooth, with minimal wave interactions occurring, as indicated in Fig. 8b at $t = 29.48$ μs. The shock subsequently passes through the throat at $t = 41.37$ μs, at which time combustion is nearly complete and therefore unaffected by the impinging shock wave that is eventually reflected off the rear actuator surface. Pressure fields become complex after the shock passes through the port, as indicated in Fig. 8c at $t = 70.76$ μs. Complete combustion occurs at $t_{\text{burn}} = 59.93$ μs, and the piston reaches its stroke at $t_{\text{stk}} = 93.74$ μs. Because of the abrupt stop of the piston at stroke, a compression wave forms and propagates back through the expansion chamber, as shown in Fig. 8c at $t = 95.30$ μs.

It is both convenient and insightful to analyze the temporal variation in average pressure within the actuator and expansion chamber, given by

$$\bar{p}_a(t) = \frac{1}{V_a(t)} \int_{-L_e(t)}^{0} p(x,t)A(x)\,\mathrm{d}x, \qquad \bar{p}_{\text{ec}}(t) = \frac{1}{V_{\text{ec}}(t)} \int_{0}^{L_p(t)} p(x,t)A(x)\,\mathrm{d}x \tag{49}$$

where

$$V_a(t) = \int_{-L_e(t)}^{0} A(x)\,\mathrm{d}x, \qquad V_{\text{ec}}(t) = \int_{0}^{L_p(t)} A(x)\,\mathrm{d}x$$

Note that the actuator gas volume extends from the explosive boundary to the port (i.e., $L_e(t) \le x \le 0$), whereas the expansion-chamber volume extends from the port to the piston surface (i.e., $0 \le x \le L_p(t)$). These integrals are evaluated numerically using the trapezoidal rule.

Figure 9 shows the average actuator and expansion-chamber pressure histories. The actuator rapidly pressurizes to a maximum

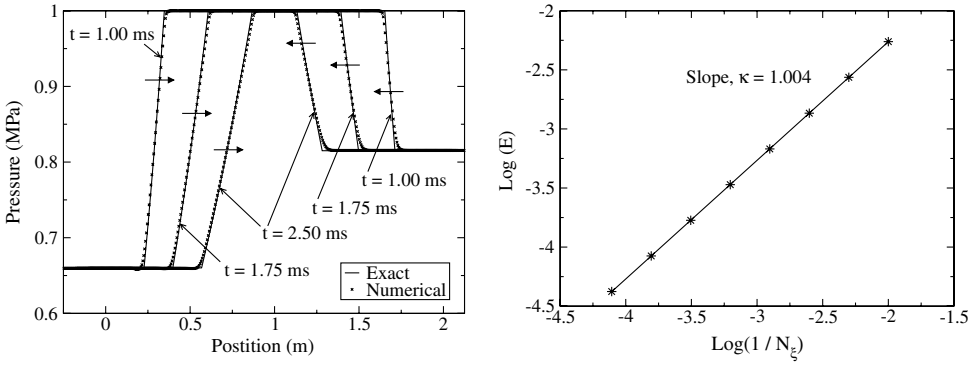

a) b)

Fig. 7 Comparison of the analytical and numerical solutions for the retracting pistons problem at $t = 1.00$, 1.75, and 2.50 ms: a) pressure and b) convergence-rate data.

Table 4 Parameter values and initial conditions used for the baseline valve configuration

Parameter or initial condition	Value	Units	Ref.
	Gas-dynamic model		
a	2.926×10^{-7}	$\mathrm{Pa}^{-0.8}$ m/s	[31]
D_a	7.988	mm	——
D_{ec}	12.744	mm	——
D_t	3.776	mm	——
L_e^0	0.750	mm	——
L_p^0	7.932	mm	——
$L_p(t_{\mathrm{stk}})$	13.932	mm	——
m_e^0	150.0	mg	——
m_p	8.0	g	——
m_v	164.0	g	——
n	0.8	——	[31]
N_e	10,000	grains	[20]
N_ξ	2,000	——	——
p^0	100.0	kPa	——
q	5.84	MJ/kg	[32]
R	337.59	$\mathrm{J/(kg \cdot K)}$	——
T^0	300.0	K	——
γ	1.235	——	——
ϑ	1.2	——	——
ρ_e^0	1910.0	$\mathrm{kg/m^3}$	[32]
	Piston resistance model		
E_h	214.0	GPa	[20]
E_p	200.0	GPa	[20]
H_h	0.35	——	[20]
H_p	0.00	——	[20]
$\hat{L}_p$	2.54	mm	[20]
r_{hi}	5.969	mm	[20]
r_{ho}	12.700	mm	[20]
tk	0.6429	mm	[20]
θ	9.0	deg	[20]
μ_b	0.088	——	[20]
μ_s	0.400	——	[20]
ν_h	0.3	——	[20]
ν_p	0.3	——	[20]
σ_{h0}	344.7	MPa	[20]
σ_{p0}	1089.0	MPa	[20]

value near 800 MPa at $t \approx 12$ μs, due to the combined effects of explosive mass and energy release by combustion and choked flow through the port. The actuator pressure then decreases, due to the increasing volume associated with the regressing explosive boundary, and mass flow continues through the port and into the expansion chamber. The expansion chamber pressurizes more slowly than the actuator, due to both its larger volume and choked flow at the port throat. Though the choked state at the actuator port evolves with time, the port remains choked for approximately

$$\frac{\bar{p}_a}{\bar{p}_{\mathrm{ec}}} \geq \left(\frac{\gamma+1}{2}\right)^{\frac{\gamma}{\gamma-1}} = 1.79$$

corresponding to $t \leq 30$ μs. The average pressures nearly equilibrate at $t \approx 37$ μs and both subsequently decrease due to volume increases with piston motion. Figure 9 also shows the instantaneous minimum and maximum pressure values within the actuator and expansion chamber to highlight fluctuations about the mean due to gas waves. For approximately $t \leq 40$ μs, few spatial fluctuations are observed in the actuator as the maximum pressure remains close to the average value. During much of this time, the minimum actuator pressure occurs at the port, which remains choked, and is significantly lower than the average value, due to the high gas velocity at that location. Similarly, as the expansion chamber pressurizes, its maximum pressure occurs at the port for approximately $t \leq 30$ μs, as shown in Fig. 9b. The minimum expansion chamber pressure deviates significantly from the average during this time. Subsequently, the spatial locations of the minimum and maximum pressure vary significantly, due to complex gas-wave interactions.

The predicted piston-velocity and force histories for the baseline configuration are shown in Fig. 10a. The piston velocity increases from rest only after the lead startup shock impinges upon it at $t \approx 6$ μs. Because of piston resistance and inertia, its velocity smoothly increases to a maximum value of 150 m/s at stroke, despite the highly transient pressure force acting on its boundary. The magnitude of this pressure force exceeds the piston-bore resistance force throughout the stroke, resulting in a complex net positive force acting on the piston. The predicted resistive force is both qualitatively and quantitatively similar to that predicted by Braud et al. [20], based on a spatially homogeneous model.

Figure 10b shows the pyrotechnic shock profile for the baseline valve; the right axis expresses the shock in terms of gravity [i.e., $F_{\mathrm{pyro}}(t)/(m_v \cdot 9.81\ \mathrm{m/s^2})$, where m_v is the mass of the valve's housing]. The sign of this shock identifies its direction. Initially, the pyrotechnic shock is dominated by high gas pressure within the combustion zone. As combustion proceeds and the valve pressurizes, the magnitude of the pyrotechnic shock increases, with large oscillations occurring due to the combined effects of piston–bore interactions and gas-wave interactions with the valve's curved

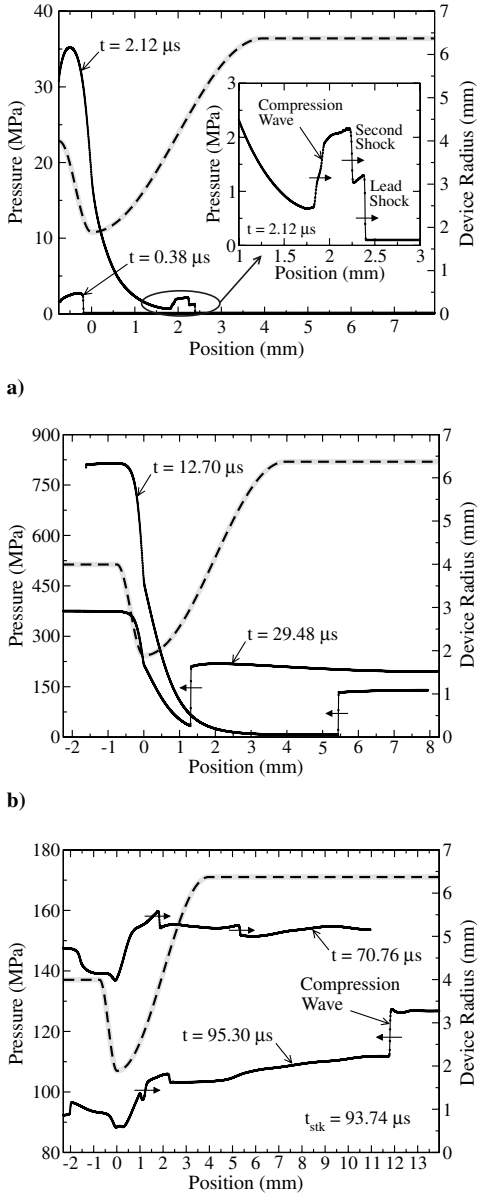

Fig. 8 Predicted pressure fields for the baseline valve: a) early, b) intermediate, and c) late times.

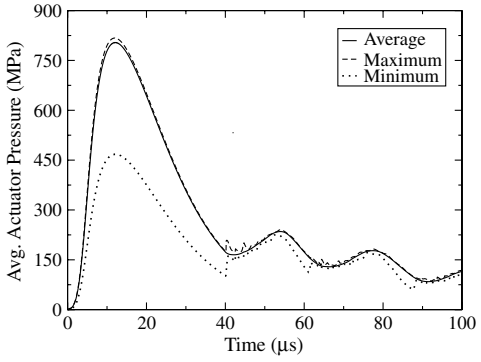

a)

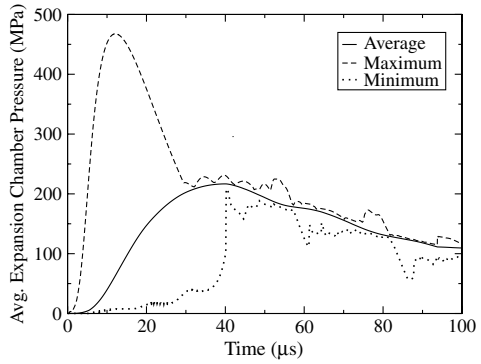

b)

Fig. 9 Predicted spatially averaged gas-pressure histories for the baseline valve: a) actuator and b) expansion chamber. Also shown are the instantaneous minimum and maximum pressures within the actuator and expansion chamber.

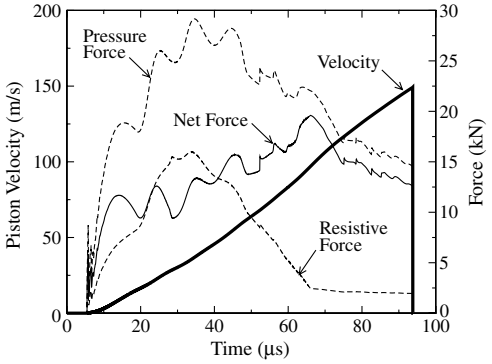

a)

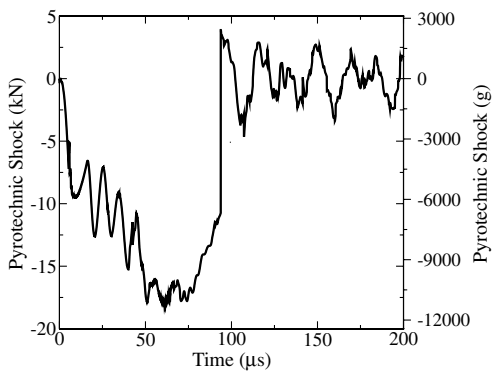

b)

Fig. 10 Predicted a) piston-velocity and force histories and b) pyrotechnic shock for the baseline valve.

surface near the port. A maximum pyrotechnic force of approximately -18 kN $(-11,188\ g)$ is predicted at $t \approx 60\ \mu$s. Subsequently, the pyrotechnic shock slightly decreases before stroke ($t_{\text{stk}} = 93.74\ \mu$s) as gas waves weaken, due to increasing gas volume induced by piston motion down the bore. The abrupt decrease in pyrotechnic shock occurring at $t = t_{\text{stk}}$ results from the impact of the piston against the stops. The impact event causes the shock to change direction and also excites the gas-dynamic fields, resulting in large-amplitude oscillations (ringing). These oscillations very slowly decay with time as the pressure waves equilibrate, though this is not evident over the short time scale shown in the figure.

We now compare the predicted average expansion-chamber pressure and piston-velocity histories with the experimental gas gun data of Decroix et al. [33] for the baseline valve considered in this study. Pressure data were recorded by a transducer located within the expansion chamber; no experimental data are currently available for the actuator, due to the extreme environment created by the explosive burn. Figure 11a shows the predicted and measured expansion-chamber pressure histories. The high-frequency fluctuations in the experimental data are likely due to unwanted noise. Although our model overpredicts the measured pressure, it reasonably predicts the pressurization rate and the low-frequency oscillations observed during stroke. A peak pressure of approximately 215 MPa is predicted at $t \approx 40\ \mu$s, whereas a peak value of approximately 170 MPa is measured by the experiments at $t \approx 40\ \mu$s. The predicted pressure history for the limiting case of zero piston resistance is also shown to illustrate how piston inertia alone affects device operation. The zero-resistance case still results in a higher peak pressure and a higher depressurization rate than the measured value. Differences between the predicted and measured profiles are possibly due to the simplified valve geometry used in this study and/or complex thermodynamic effects. Although speculative, this discrepancy may also be due to incomplete explosive burn in the experiments, which would induce lower pressures. Assuming that 5% of the initial explosive mass remains unburned ($\approx$7.5 mg), then the peak expansion-chamber pressure would be reduced by approximately 15 MPa, based on the initial chamber volume and an average chamber temperature of 3500 K. Moreover, postfire evaluation of valve actuators indicates the existence of small amounts of explosive residue, though this residue has not been chemically analyzed or weighed, to our knowledge. A detailed examination of how explosive mass affects expansion-chamber pressurization is given in the following section.

In the apparatus used to measure the piston-velocity history, the back end of the valve bore was extended and slightly modified to enable optical access to the piston by a VISAR system (velocity interferometer system for any reflector). Additionally, the piston stops were removed to enable the piston to travel beyond its normal stroke distance. Both the actuator and piston used in the experiments are identical to that used in the actual valve. Figure 11b shows the measured and predicted piston-velocity histories; here, the simulations were allowed to continue beyond t_{stk} to enable longer time comparisons with the data. The high-frequency fluctuations in the experimental data are possibly due to waves within the solid piston that are recorded by the highly sensitive VISAR system. Overall, the model reasonably predicts the measured piston-velocity history. The case of zero piston resistance substantially overpredicts piston velocity during stroke.

V. Parametric Analysis

In this section, we characterize the sensitivity of our model to independent variations in key parameters. In particular, we focus on burn-rate parameters, because they directly control gas power production within the valve and there is uncertainty in their values under the extreme conditions of actuation. We also focus on parameters that are important from a design perspective, including port cross-sectional area and explosive mass. The model sensitivity to other constitutive and geometric parameters is characterized in [25].

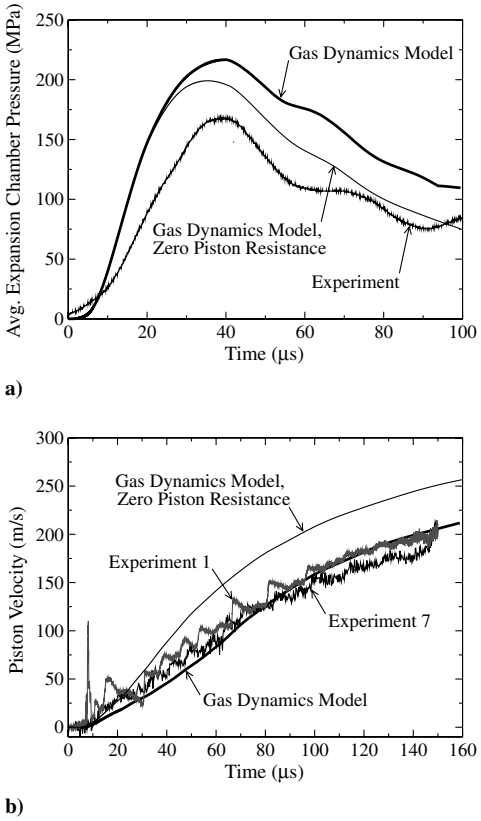

Fig. 11 Comparisons with experimental data: a) spatially averaged expansion-chamber pressure and b) piston-velocity histories.

A. Burn-Rate Parameters

The location of the explosive boundary within the actuator evolves based on Eq. (16); this expression depends on both the pressure-dependent explosive-burn rate r_e, given by the first expression of Eq. (15), and the collective surface area A_e of N_e simultaneously burning spherical explosive grains, given by the last expression of Eq. (15). Values for the burn-rate prefactor a and exponent n are usually determined based on closed-bomb experiments. In this study, baseline values for a and n were taken from the literature for the explosive HMX [31], and the baseline value for N_e was chosen so that predictions for the firing of an actuator containing 150 mg of HMX into a 1 cm^3 rigid vessel match experimentally measured pressure histories [20].

We first vary the burn-rate exponent over the range $0.70 \leq n \leq 0.86$ and fix all remaining parameters, including the burn-rate prefactor, at their baseline values. Many explosives and propellants have values of n that fall within this range [31,34]. The predictions are summarized in Fig. 12; curves in Figs. 12a–12c are terminated when both combustion and stroke are complete. Figure 12a shows predicted histories for the mass fraction of burned explosive m_e^0, where a value of unity corresponds to complete combustion. Figures 12b and 12c show the average actuator and expansion-chamber pressure histories. The explosive rapidly burns for large values of n, with only marginal variations in the predictions relative to the baseline case. The largest value of $n = 0.86$ exhibits fast actuator pressurization with a peak average pressure of approximately 1330 MPa. The corresponding combustion and stroke times of $t_{\text{burn}} = 11.86$ μs and $t_{\text{stk}} = 86.53$ μs are the smallest for the range of n values considered. Slower burn rates are predicted for decreasing values of n, resulting in lower actuator pressurization rates, lower peak pressures, and higher combustion and stroke times. For example, the complete combustion and stroke times predicted for $n = 0.70$ are $t_{\text{burn}} = 1183.61$ μs and $t_{\text{stk}} = 436.36$ μs. As shown in Fig. 12c, similar trends are observed for the average expansion-chamber pressure histories, except for $n \geq 0.84$, due to choked gas

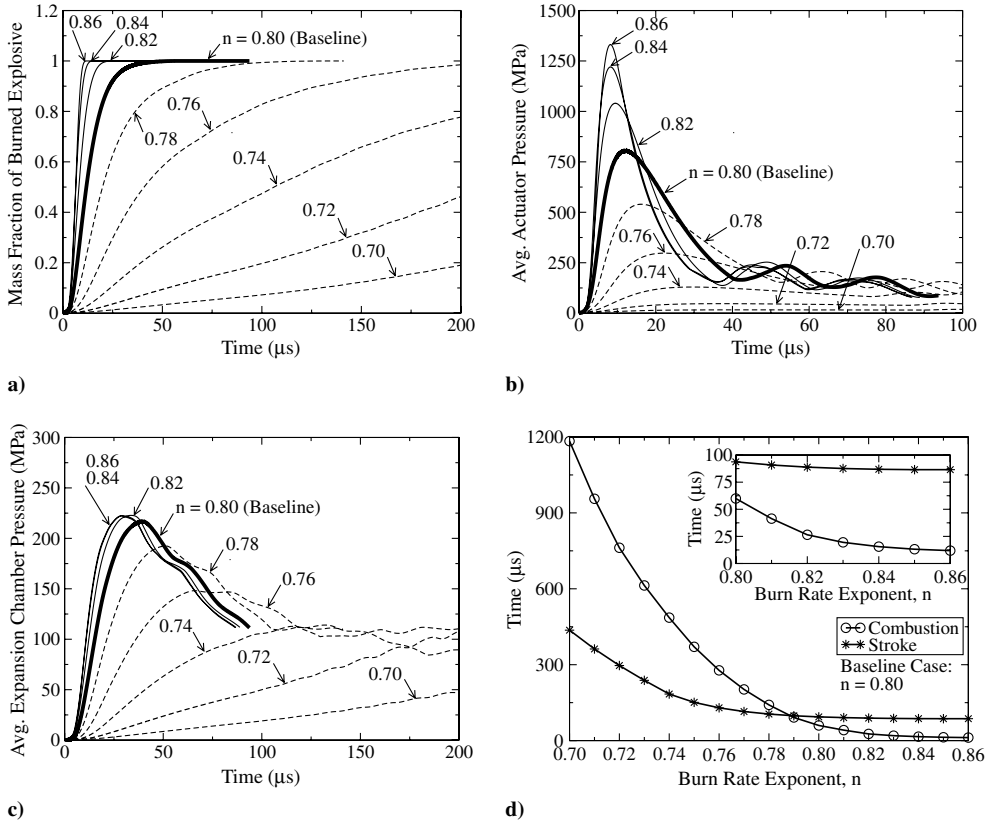

Fig. 12 Predicted time histories for the burn-rate exponent study: a) mass fraction of burned explosive, average b) actuator and c) expansion-chamber pressures. d) Summary of the predicted variation in complete combustion and stroke times with burn-rate exponent.

flow through the port that restricts expansion-chamber pressurization. The predicted variations in complete combustion and stroke times with n are summarized in Fig. 12d. Both the combustion and stroke times asymptotically approach minimum values with increasing n. The combustion time approaches a minimum value of $t_{\text{burn}} \approx 11$ μs, whereas the stroke time approaches a minimum value of $t_{\text{stk}} \approx 87$ μs. The baseline stroke time, $t_{\text{stk}} = 93.74$ μs, is only 8% greater than this minimum value, and the stoke times for $n \geq 0.79$ are within 15% of this value. As such, stroke time is mostly sensitive to changes in burn-rate exponent for $n < 0.79$.

We now consider variations in burn-rate prefactor over the range

$$0.20 \times 10^{-7} \leq a \leq 8.00 \times 10^{-7} \text{ m/s Pa}^{-0.8}$$

Most explosives and propellants have values that fall within this range [31,34]. The predicted results are qualitatively similar to those presented for the burn-rate exponent in that larger values of a result in rapid combustion. Peak average pressures near 1275 and 225 MPa, respectively, are predicted within the actuator and expansion chamber for the largest value considered, $a = 8.00 \times 10^{-7}$ m/s Pa$^{-0.8}$, whereas lower peak pressures and pressurization rates are predicted for decreasing values of a. The complete combustion and stroke times again asymptotically approach minimum values with increasing a, with the combustion time exhibiting greater sensitivity, as shown in Fig. 13a. The minimum stroke time is $t_{\text{stk}} \approx 87$ μs, with little variation predicted for $a \geq 2.926 \times 10^{-7}$ m/s Pa$^{-0.8}$.

Next, we characterize how the number of burning explosive grains N_e affects predictions for the baseline valve configuration. This parameter arguably contains the most uncertainty of all model parameters; grains will likely fracture due to the extreme actuator environment following ignition, and it is prohibitively difficult to directly measure this quantity based on observation. Here, the number of burning grains is varied over the range $100 \leq N_e \leq 250,000$; all remaining parameters, including the explosive mass, are fixed at their baseline values. As such, the grain radius will vary over the corresponding range $572 \geq R_e \geq 42$ μm (the baseline value $N_e = 10,000$ corresponds to $R_e = 123$ μm). Relative to the baseline value, the burn surface area decreases by approximately 78.5% for $N_e = 100$ and increases by approximately 192.4% for $N_e = 250,000$. The predictions are again qualitatively similar to those for the burn-rate parameters already considered. Rapid combustion is predicted for large values of N_e, due to increased burn surface area, resulting in high peak pressures and pressurization rates. Predicted average expansion-chamber pressure histories are almost identical for $N_e \geq 100,000$. Predictions for the complete combustion and stroke times, summarized in Fig. 13b, asymptotically approach minimum values of $t_{\text{burn}} = 10$ μs and $t_{\text{stk}} \approx 87$ μs, with the combustion time exhibiting greater sensitivity. Stroke time predictions for $N_e \geq 5,000$ are within 15% of this minimum value.

In summary, independent variations in the explosive-burn-rate parameters a, n, and N_e about their baseline values, which were chosen based on physically plausible arguments, result in qualitatively similar responses. Reasonably large variations in these parameters result in only small changes in piston stroke time and velocity; as such, marginal uncertainty in the burn rate is not likely to significantly alter valve performance.

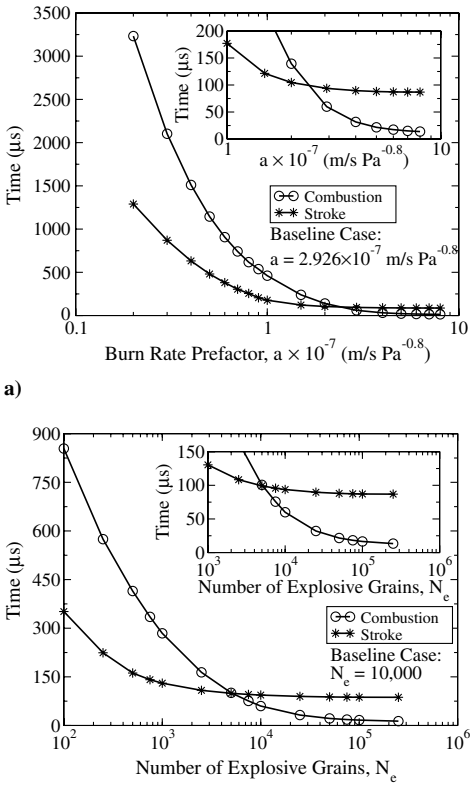

Fig. 13 Summary of the predicted variation in complete combustion and stroke times with a) burn-rate prefactor and b) number of explosive grains.

B. Design Parameters

Valve geometry and explosive mass represent some of the most important features from a design perspective. Many geometric parameters exist, even for our simplified valve, including the actuator length and diameter, the expansion-chamber length and diameter, and the piston mass and shape, just to list a few. Here, we focus on characterizing the effect of port diameter on valve performance, because it plays a particularly critical role in controlling pressurization of both the actuator and expansion chamber. We also examine how explosive mass affects performance, because it is often difficult to a priori determine the minimum mass needed for successful valve operation; the use of excessive mass may result in undesirable consequences.

To assess the effect of port diameter, we define a port scale factor by $s_t \equiv D_t/D_t^*$, where D_t^* denotes the baseline diameter given in Table 4; the baseline valve configuration corresponds to $s_t = 1.0$. We consider variations over the range $0.125 \leq s_t \leq 1.875$. Figures 14a and 14b show the average actuator and expansion-chamber pressure histories for several values of s_t. Small ports, with approximately $s_t < 0.5$, exhibit large peak actuator pressures and pressurization rates, due to the combined effects of restricted gas flow into the expansion chamber and pressure enhanced combustion. Larger ports, with approximately $s_t > 1.5$, exhibit slow actuator pressurization, due to mostly unobstructed gas flow through the port, resulting in lower burn rates. Fastest expansion-chamber pressurization occurs for the baseline configuration, in which a peak pressure of approximately 215 MPa is predicted at $t \approx 40$ μs. Thus, valves with either large or small port cross-sectional areas, relative to the baseline configuration, result in slower expansion-chamber pressurization. The extent to which port diameter was optimally selected based on analysis and experimentation during valve development is unclear to the authors. It is important to emphasize that the model was not tuned to obtain this result.

Figure 15a gives corresponding predictions for piston-velocity history. In addition to longer stroke times, valves with extreme values of s_t exhibit irregular piston-velocity histories. For example, the piston velocity for $s_t = 0.125$ exhibits mild oscillatory behavior until $t \approx 250$ μs before accelerating to stroke. Close inspection of the piston velocity for $s_t = 1.875$ also indicates slightly irregular features, due to strong gas-dynamic–wave interactions at the piston surface. Though all cases result in successful valve operation, those possessing irregular motion are undesirable from a design perspective. Figure 15b summarizes the predicted combustion and stroke times. Valves with $s_t < 1$ exhibit faster combustion times, due to higher actuator pressurization rates induced by restricted gas flow through the smaller ports. Though small ports result in higher combustion-energy release rates, slower convective transport of this energy to the expansion chamber increases stroke time. Valves with

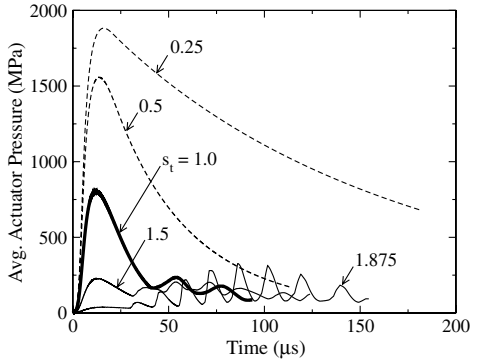

a)

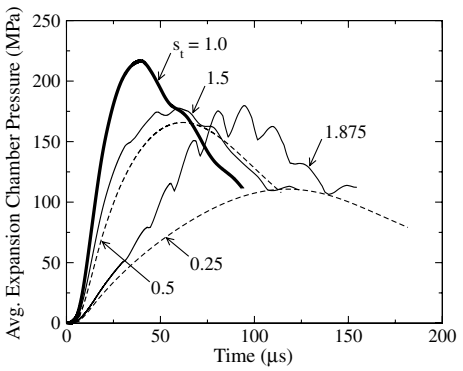

b)

Fig. 14 Predicted average a) actuator and b) expansion-chamber pressure histories for the scaled port study.

$s_t > 1$ facilitate convective transport to the expansion chamber, but reduce the combustion rate by limiting actuator pressurization. These predictions indicate that the baseline configuration results in optimal performance based on stroke time. Corresponding pyrotechnic shock histories for $s_t = 0.25$, 1.0, and 1.875 are shown in Fig. 15c. High-frequency oscillations are observed for $s_t = 0.25$, due to repeated wave reflections between the explosive boundary and the actuator side of the port, though the shock magnitude is relatively low. Fewer oscillations are predicted for larger values of s_t, due to less restricted flow through the port, but the shock magnitude increases. A peak force of approximately -26 kN $(-16,161$ g) at $t \approx 105$ μs is reached for the extreme case of $s_t = 1.875$. These significant differences in pyrotechnic shock signature suggest that nonintrusive shock measurements can potentially diagnose whether or not a valve port has been accidentally obstructed by actuator/explosive debris.

To assess the effects of explosive mass, we define a mass scale factor by $s_e \equiv m_e/m_e^*$, where m_e^* is the baseline value given in Table 4. For this analysis, we consider the range $0.25 \leq s_e \leq 3.0$, which corresponds to $37.5 \leq m_e \leq 450.0$ mg. The explosive-grain size (i.e., $R_e \approx 123$ μm) is fixed, whereas the number of explosive grains N_e varies based on the given mass. Further, the initial clearance length (volume), defined as the distance (volume) between the initial explosive boundary and the port throat, is fixed for consistency. The final actuator length, therefore, will also vary based on the explosive mass. Figures 16a and 16b show the average actuator and expansion-chamber pressure histories. Large values of s_e exhibit high peak pressures and pressurization rates, due to larger gas mass and energy production. For $s_e = 3.0$, peak pressures of approximately 1580 MPa at $t \approx 13$ μs and 440 MPa at $t \approx 37$ μs are predicted in the actuator and expansion chamber, respectively.

Corresponding piston-velocity histories are shown in Fig. 17a. The largest explosive mass results in the shortest stroke time of $t_{\text{stk}} = 64.17$ μs, with a maximum velocity of 245 m/s. The piston stroke time increases, and velocity decreases, with decreasing s_e. Irregular piston motion results for $s_e \leq 0.5$, due to insufficient energy release; in fact, the piston unsuccessfully strokes for

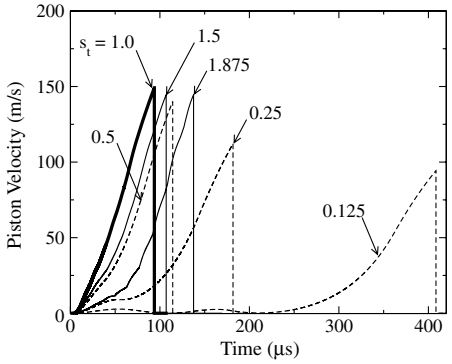

a)

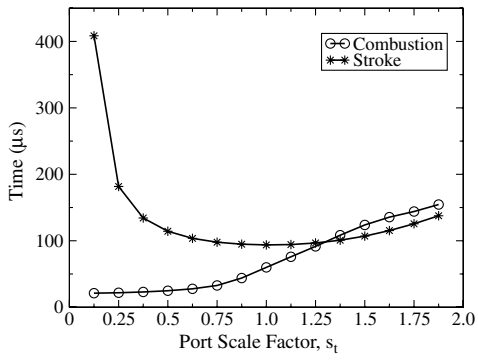

b)

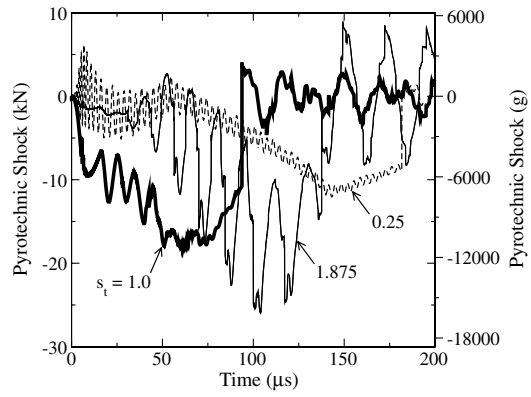

c)

Fig. 15 Predicted a) piston-velocity histories, b) combustion and stroke times, and c) pyrotechnic shocks for the port study.

$s_e = 0.25$, resulting in valve failure. The complete combustion and stroke times are summarized in Fig. 17b. Valves with large values of s_e exhibit fast combustion and stroke times, but they produce large pyrotechnic shocks, as shown in Fig. 17c. For $s_e > 2$, only a marginal gain in stroke time is obtained with a large increase in pyrotechnic shock. The largest case considered ($s_e = 3.0$) produces an intense pyrotechnic shock with a peak force of approximately -48 kN $(-29,835\ g)$ at $t \approx 51$ μs and large-amplitude oscillations following piston stroke. These predictions indicate that excessive explosive mass, while seemingly beneficial in terms of stroke time and velocity, may produce unacceptably strong pyrotechnic shocks.

VI. Miniature Valves

In this section, we examine how valve performance varies with a linear reduction in size relative to the baseline configuration. All valves considered here are geometrically similar, with dimensions specified by a uniform scale factor that is defined by $s \equiv l/L$, where L is a baseline dimension and l is the corresponding dimension of the

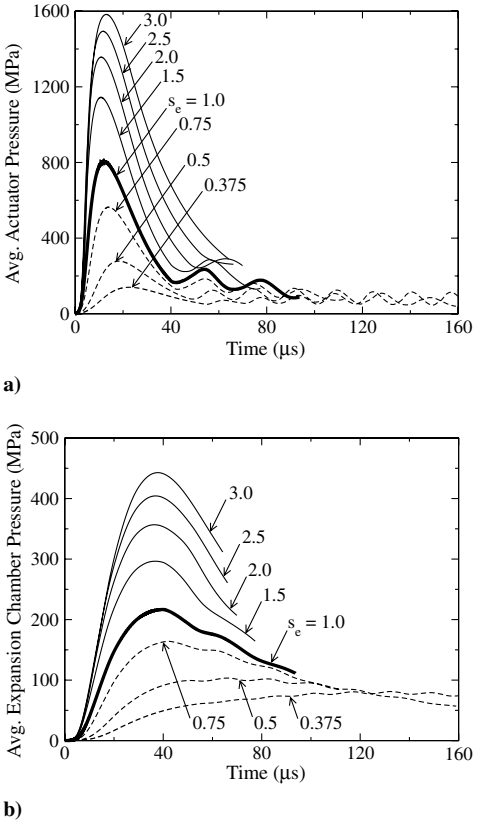

Fig. 16 Predicted average a) actuator and b) expansion-chamber pressure histories for the explosive mass study.

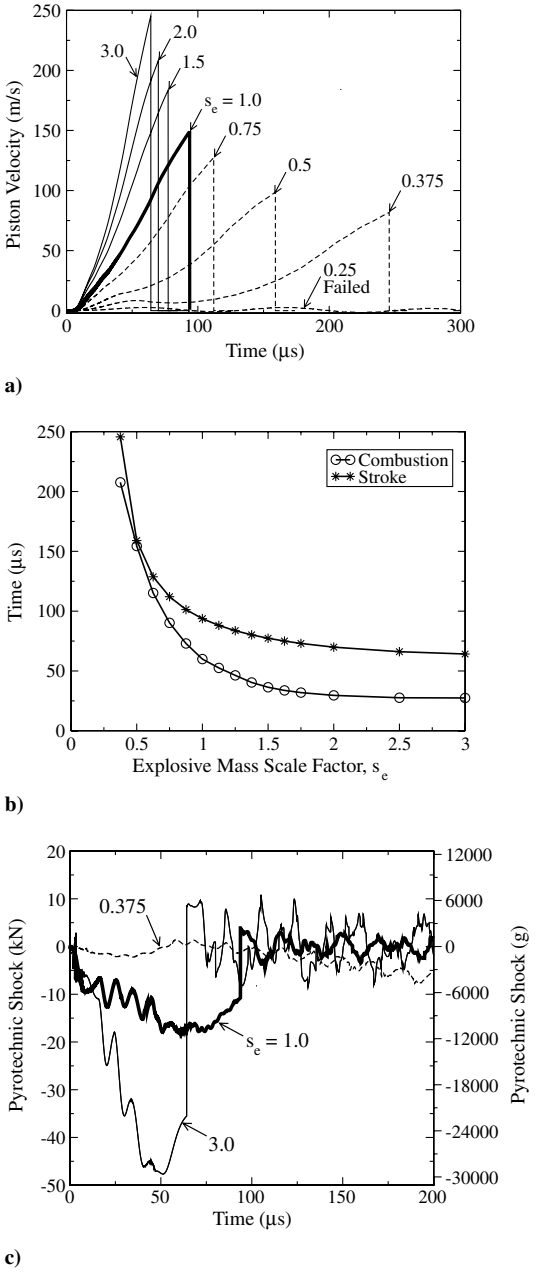

Fig. 17 Predicted a) piston-velocity histories, b) complete combustion and stroke times, and c) pyrotechnic shock histories for the explosive mass study.

scaled valve; the baseline configuration corresponds to $s = 1.0$. We consider the range $0.125 \leq s \leq 1.0$ and assume ad hoc that the ignition process produces burning grains of roughly the same initial size for all cases. The number of burning grains is computed based on the explosive mass and scaled actuator volume. All remaining parameters are fixed at their baseline values. Scale-dependent tribology and material properties are not accounted for in this analysis; as such, it gives only leading-order predictions for the variation in valve operation and performance with size.

In this study, valves are categorized based on the terminology introduced by Gonthier et al. [35]. Three categories exist that which depend on the piston-velocity history: *overdriven*, *transitional*, and *underdriven*. Overdriven valves have piston-velocity histories that are largely insensitive to scale, whereas those of underdriven valves are irregular and depend on scale. Transitional valves refer to those that border underdriven-valve behavior in terms of scale and represent a practical design limit for these geometrically similar valves. This terminology is not meant to imply, however, that the corresponding explosive energy release for underdriven valves is insufficient to overcome the integrated work required for stroke; rather, it simply refers to the onset of irregular piston motion.

Figures 18a and 18b show the predicted piston position and velocity histories for several values of s; here, the histories are truncated following piston stroke for clarity. Valves corresponding to $0.75 \leq s \leq 1.0$ are overdriven in that their velocity histories smoothly increase with time through stroke. The predicted stroke time for these valves ranges from $t_{\text{stk}} = 93.74$ μs for $s = 1.0$ to 75.77 μs for $s = 0.75$, corresponding to stroke lengths of 6.0 and 4.5 mm, respectively. Underdriven valves are predicted for $0.125 \leq s \leq 0.4375$, because their initial piston-velocity behavior is irregular. For example, the velocity history for $s = 0.3125$ initially increases quickly, then slowly increases for a small time period (approximately $20 \leq t \leq 30$ μs) before quickly increasing again to a final value of 115 m/s at $t_{\text{stk}} = 62.75$ μs; this irregular behavior is more pronounced for smaller values of s. In fact, pistons corresponding to $0.23 < s < 0.30$ even decelerate for part of their motion, as shown in Fig. 18b for $s = 0.25$ ($20 \leq t \leq 30$ μs).

Figures 18c and 18d show the average actuator and expansion-chamber pressure histories. As shown in the figures, peak actuator pressures decrease significantly with decreasing values of s. Overdriven valves attain peak values of $615 \leq \bar{p}_a \leq 800$ MPa before depressurizing due to gas flow through the port; peak expansion-chamber pressures are in the range $200 \leq \bar{p}_{\text{ec}} \leq 215$ MPa. Underdriven valves exhibit low actuator pressurization rates, due to rapid gas flow through the port relative to the burn rate.

Figure 19 summarizes the predicted scale-dependent variation in mass specific piston kinetic energy at stroke and the complete combustion and stroke times. These plots clearly illustrate key differences between overdriven and underdriven valves. Overdriven valves are characterized by complete, or nearly complete, explosive combustion before piston stroke, whereas underdriven valves are characterized by significantly higher combustion times relative to their stroke times. Moreover, the mass specific piston kinetic energy at stroke is largely scale-independent for overdriven valves and is nonmonotonically scale-dependent for underdriven valves.

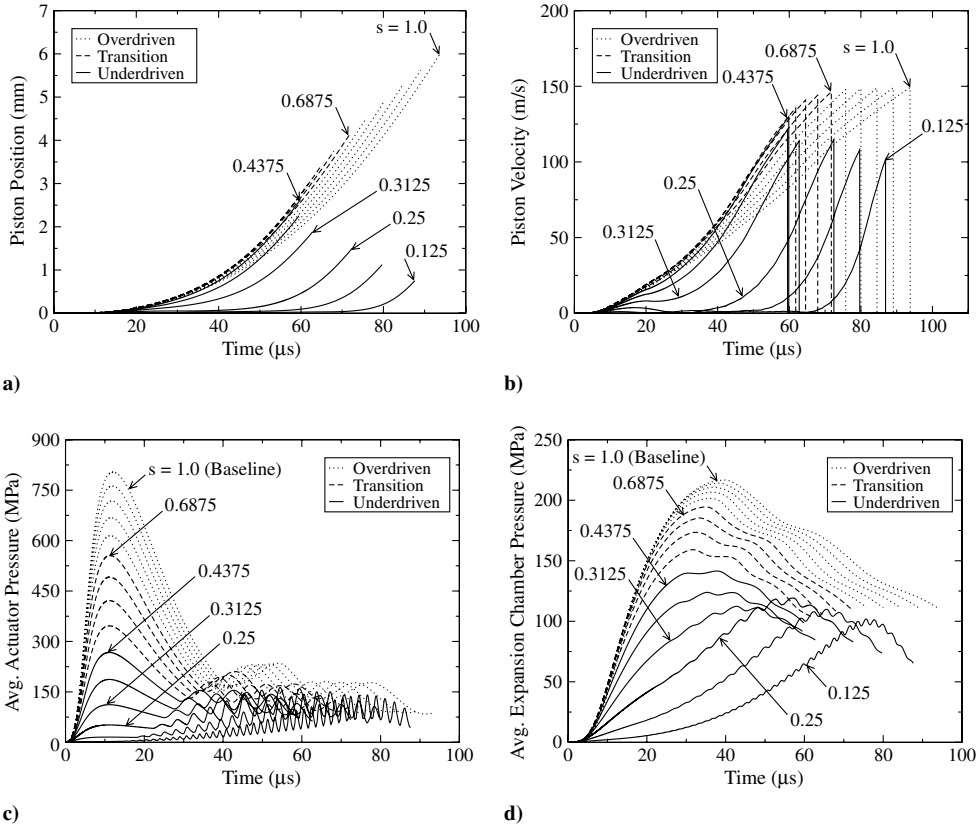

Fig. 18 Predicted histories for a) piston position, b) piston velocity, c) average actuator pressure, and d) average expansion-chamber pressure for geometrically scaled valves.

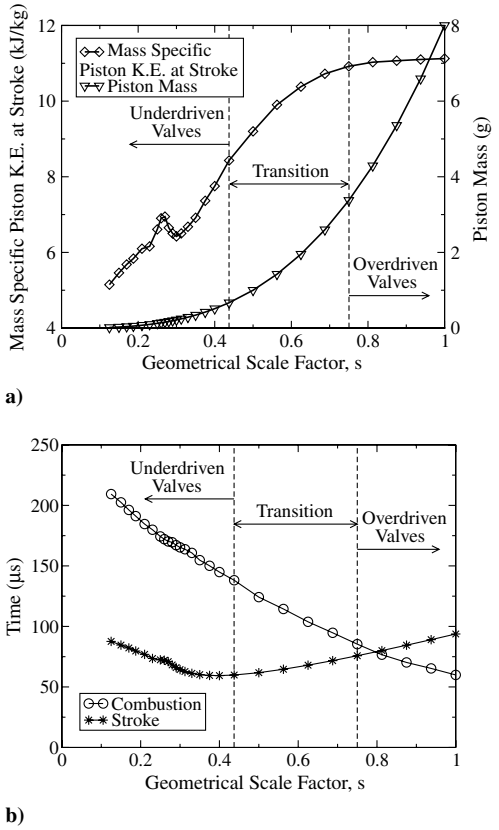

Fig. 19 Summary of the predicted variation in a) mass specific piston kinetic energy at stroke and b) complete combustion and stroke times with geometric scale factor.

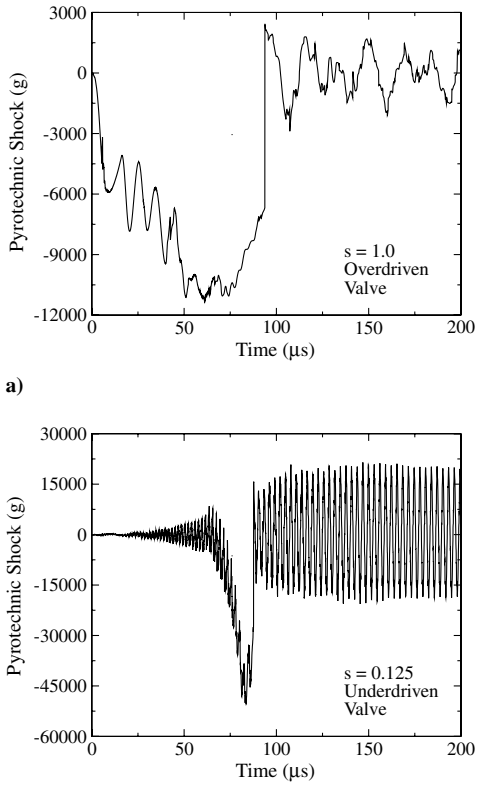

Fig. 20 Predicted pyrotechnic shock histories for geometrically scaled valves corresponding to a) $s = 1.0$ and b) $s = 0.125$.

Finally, pyrotechnic shock predictions for $s = 1.0$ and 0.125 are shown in Fig. 20. For small values of s, the shock signature consists of high-amplitude, high-frequency fluctuations resulting from strong gas-wave interactions. As shown in Fig. 20b, the smallest valve considered in this study ($s = 0.125$) induces the strongest shock. Because electronic components are sensitive to both shock magnitude and frequency, these predictions indicate that care should be exercised in the design and development of miniature valves for aerospace applications.

VII. Conclusions

A transient quasi-1-D model was formulated and numerically implemented to characterize the operation and performance of explosively actuated valves. The model accounts for acoustic energy transport within and between actuator and expansion-chamber volumes, gas-wave interactions with both the burning explosive surface and the piston boundary, mechanical interference due to elastic–plastic contact between the piston and valve bore, valve cross-sectional area variations, and gas volume changes due to solid explosive combustion and piston motion. The IBVP was numerically integrated in terms of generalized coordinates using a TVD high-resolution shock-capturing technique.

Predictions for a baseline valve configuration agree reasonably well with experimental data for piston stroke time, expansion-chamber pressure and pressurization rate, and piston velocity. Though complex pressure fields are predicted within the valve, piston motion is largely insensitive to the gas-dynamic pressure force acting on its surface, due to inertia and piston-bore resistance. Further, pressure-dependent explosive burn within the actuator is largely unaffected by product-gas waves emanating from the expansion chamber, due to mass choking at the port.

The effect of independent variations in key model parameters, relative to their baseline values, on valve performance was examined. Predictions indicate that port cross-sectional area, an important design parameter, controls both the combustion-energy release rate and expansion-chamber pressurization rate. Valves with large ports release combustion energy slowly, due to mostly unobstructed flow of product gas into the expansion chamber, resulting in long stroke times. Valves with small ports experience slow expansion-chamber pressurization, due to obstructed gas flow through the port, resulting in both irregular piston motion and long stroke times. The port area for the baseline configuration results in optimal performance in terms of both piston motion and stroke time. Variations in explosive mass, another key design parameter, were also shown to significantly affect both valve performance and pyrotechnic shock. Valves with too little mass experience irregular piston motion, whereas large mass results in a large pyrotechnic shock and only minimal improvement in piston motion and stroke time over the baseline configuration.

An analysis of small valves, corresponding to a linear reduction in size relative to the baseline configuration, identified three performance categories that depend on scale: overdriven, transitional, and underdriven. Overdriven valves (with $0.75 \leq s \leq 1.0$, where the scale factor $s = 1$ corresponds to the baseline configuration) result in optimal performance characterized by smooth, regular, piston motion and short stroke time, with relatively mild pyrotechnic shock. These valves experience both rapid combustion and expansion-chamber pressurization and have a mass specific piston kinetic energy at stroke that is scale-independent. Underdriven valves ($0.125 \leq s \leq 0.4375$) result in irregular piston motion and very large, high-frequency, pyrotechnic shocks that should be carefully considered in the design and development of miniature valves for aerospace applications. Transitional valves ($0.4375 < s < 0.75$) border underdriven-valve behavior and represent a practical design limit for these geometrically similar valves.

Several modeling improvements can be made to better reflect actual valve behavior. For example, the burst disc that hermetically seals the explosive within the actuator before operation and enables pressure build immediately following ignition was ignored in this study. Inclusion of this disc in the model would be straightforward and may cause a stronger starting shock to propagate through the expansion chamber and impact the piston, thereby affecting its initial velocity. The simple combustion zone model formulated in this study may also be modified to account for the dispersal of burning explosive grains throughout the actuator and expansion-chamber volumes. Such a modification, however, would likely require a considerably more complex description based on a multiphase-field theory, similar to that formulated by Baer and Nunziato [36] and Bdzil et al. [37], to describe detonation transition in granular explosives.

Acknowledgments

The authors gratefully acknowledge the W-Division, Detonator Design (W-6), and Gas Transfer Systems (W-7) Groups of Los Alamos National Laboratory for funding this work. The contract monitor is Nathan Burnside. They would also like to acknowledge Michele Decroix (D-6) and Brett Okhuysen (D-3) of the Decision Applications Division of Los Alamos National Laboratory for helpful discussions in support of this work.

References

[1] Bement, L. J., and Schimmel, M. L., "A Manual on Pyrotechnic Design, Development, and Qualification," NASA TM 110172, June 1995.

[2] Oldham, A. H., "Explosively Actuated Tools," *Journal of the Army Ordnance Association*, Vol. 18, No. 108, 1938, pp. 361–366.

[3] Seeholzer, T. L., Smith, F. Z., Eastwood, C. W., and Steffes, P. R., *Applications Catalog of Pyrotechnically Actuated Devices/Systems*, NASA TM 106810, Washington, D.C., 1995.

[4] Simmons, W. H., *Apollo Spacecraft Pyrotechnics*, NASA TM X-58032, Washington, D.C., Oct. 1969.

[5] Billing, R., "Caging Mechanisms for the Mars Exploration Rover Instrument Deployment Device," 10th European Space Mechanisms and Tribology Symposium, ESA Paper SP-524, San Sebastián, Spain, Sept. 2003.

[6] Christensen, K. L., and Narahara, R. M., "Spacecraft Separation," *Space/Aeronautics*, Vol. 46, No. 1, 1966, pp. 74–82.

[7] Lake, E. R., Thompson, S. J., and Drexelius, V. W., "A Study of the Role of Pyrotechnic Systems on the Space Shuttle Program," NASA CR-2292, Washington, D.C., Sept. 1973.

[8] Rossi, C., Briand, D., Dumonteuil, M., Camps, T., Pham, P. Q., and Rooij, N. F., "Matrix of 10×10 Addressed Solid Propellant Microthrusters: Review of Technologies," *Sensors and Actuators A (Physical)*, Vol. 126, 2006, pp. 241–252. doi:10.1016/j.sna.2005.08.024

[9] Trimmer, W. S. N., "Microrobots and Micromechanical Systems," *Sensors and Actuators*, Vol. 19, 1989, pp. 267–287. doi:10.1016/0250-6874(89)87079-9

[10] Rossi, C., Conto, T., Estéve, D., and Larangot, B., "Design, Fabrication, and Modeling of MEMS-Based Microthrusters for Space Applications," *Smart Materials and Structures*, Vol. 10, 2001, pp. 1156–1162. doi:10.1088/0964-1726/10/6/304

[11] Rossi, C., Orieux, S., Larangot, B., Conto, T. D., and Estéve, D., "Design, Fabrication, and Modeling of Solid Propellant Microrocket—Application to Micropropulsion," *Sensors and Actuators A (Physical)*, Vol. 99, 2002, pp. 125–133. doi:10.1016/S0924-4247(01)00900-1

[12] Rossi, C., Rouhani, M. D., and Estéve, D., "Prediction of the Performance of a Si-Micromachined Microthruster by Computing the Subsonic Gas Flow Inside the Thruster," *Sensors and Actuators*, Vol. 87, 2000, pp. 96–104. doi:10.1016/S0924-4247(00)00464-7

[13] Bement, L. J., "Functional Performance of Pyrovalves," *Journal of Spacecraft and Rockets*, Vol. 34, No. 3, 1997, pp. 391–396. doi:10.2514/2.3223

[14] Ng, R., and Kwon, D. M., "Use of MAVIS II to Integrate the Modeling and Analysis of Explosive Valve Interactions for Spacecraft Applications," *Proceedings of the 1996 Autumn Seminar on Propellants, Explosives and Pyrotechnics*, Theory and Practice of Energetic Materials, Science Press, Beijing, 1996, pp. 461–477.

[15] Jones, B. K., Emery, A. F., Hardwick, M. F., and Ng, R., "Analysis of Explosively Actuated Valves," *Journal of Mechanical Design*, Vol. 116, 1994, pp. 809–815. doi:10.1115/1.2919454

[16] Kuo, J., and Goldstein, S., "Dynamic Analysis of NASA Standard Initiator Driven Pin Puller," 29th Joint Propulsion Conference and Exhibit, Monterey, CA, AIAA Paper 93-2066, June 1993.

[17] Gonthier, K. A., and Powers, J. M., "Formulation, Predictions, and Sensitivity Analysis of a Pyrotechnically Actuated Pin Puller Model," *Journal of Propulsion and Power*, Vol. 10, No. 4, 1994, pp. 501–507. doi:10.2514/3.23800

[18] Butler, P. B., Kang, J., and Krier, H., "Modeling and Numerical Simulation of the Internal Thermochemistry of Automotive Airbag Inflators," *Progress in Energy and Combustion Science*, Vol. 19, 1993, pp. 365–382. doi:10.1016/0360-1285(93)90009-4

[19] Vorozhtsov, A., Bondarchuk, S., and Kondratova, O., "Mathematical Simulation of Airbag Inflation by Low Temperature Gas Generator Products," *Propellants, Explosives, Pyrotechnics*, Vol. 25, No. 5, 2000, pp. 220–223. doi:10.1002/1521-4087(200011)25:5<220::AID-PRE-P220>3.0.CO;2-3

[20] Braud, A. M., Gonthier, K. A., and Decroix, M. E., "System Modeling of Explosively Actuated Valves," *Journal of Propulsion and Power*, Vol. 23, No. 5, 2007, pp. 1080–1095. doi:10.2514/1.27414

[21] Lee, H. S., "Unsteady Gasdynamics Effects in Pyrotechnic Actuators," *Journal of Spacecraft and Rockets*, Vol. 41, No. 5, 2004, pp. 877–886. doi:10.2514/1.2594

[22] Bateman, V. I., and Davie, N. T., "Recommended Practice for Pyroshock," *Proceedings of the 41st Annual Technical Meeting of the Institute of Environmental Sciences*, Inst. of Environmental Sciences, Mount Prospect, IL, 1995.

[23] Moening, C. J., "Views of the World of Pyrotechnic Shock," *Shock and Vibration Bulletin*, May 1985, Pt. 3, 1986, pp. 3–28.

[24] Städtke, H., *Gasdynamic Aspects of Two-Phase Flow*, Wiley-VCH, Weinheim, Germany, 2006.

[25] Paul, B. H., "Analysis of Gas-Dynamic Waves in Explosively Actuated Valves," M.S. Thesis, Louisiana State Univ., Baton Rouge, LA, 2008.

[26] Atwood, A. I., Boggs, T. L., Curran, P. O., Parr, T. P., Hanson-Parr, D. M., Price, C. F., and Wiknich, J., "Burning Rate of Solid Propellant Ingredients. Part 1: Pressure and Initial Temperature," *Journal of Propulsion and Power*, Vol. 15, No. 6, 1999, pp. 740–747. doi:10.2514/2.5522

[27] Kurganov, A., and Tadmor, E., "New High-Resolution Central Schemes for Nonlinear Conservation Laws and Convection-Diffusion Equations," *Journal of Computational Physics*, Vol. 160, 2000, pp. 241–282. doi:10.1006/jcph.2000.6459

[28] Çengel, Y. A., and Cimbala, J. M., *Fluid Mechanics: Fundamentals and Applications*, McGraw–Hill, New York, 2006.

[29] LeVeque, R. J., *Numerical Methods for Conservation Laws*, Birkhäuser–Verlag, Basel, Switzerland, 1992.

[30] Zel'dovich, Y. B., and Raizer, Y. P., *Elements of Gasdynamics and the Classical Theory of Shock Waves*, Academic Press, New York, 1968.

[31] Prasad, K., Yetter, R. A., and Smooke, M. D., "An Eigenvalue Method for Computing the Burning Rates of HMX Propellants," *Combustion and Flame*, Vol. 115, 1998, pp. 406–416. doi:10.1016/S0010-2180(98)00009-1

[32] Gibbs, T. R., and Popolato, A., *LASL Explosive Property Data*, Univ. of California Press, Berkeley, CA, 1980.

[33] Decroix, M., Quintana, D., Burnett, D., Tafoya, J. I., and Tafoya, J. M., "Investigation of Actuation Dynamics in an Explosively Actuated Valve Using a Gas Gun," 41st AIAA/ASME/SAE/ASEE Joint Propulsion Conference and Exhibit, Tuscon, AZ, AIAA Paper 2005-4036, July 2005.

[34] Luca, L. D., Cozzi, F., Germiniasi, G., Ley, I., and Zenin, A. A., "Combustion Mechanism of an RDX-Based Composite Propellant," *Combustion and Flame*, Vol. 118, Nos. 1–2, 1999, pp. 248–261. doi:10.1016/S0010-2180(98)00148-5

[35] Gonthier, K. A., Paul, B. H., Braud, A. M., and Decroix, M. E., "Modeling of an Explosively Driven Micro-Valve," 45th AIAA Aerospace Sciences Meeting and Exhibit, Reno, NV, AIAA Paper 2007-0291, Jan. 2007.

[36] Baer, M. R., and Nunziato, J. W., "A Two-Phase Mixture Theory for the Deflagration-to-Detonation Transition (DDT) in Reactive Granular Materials," *International Journal of Multiphase Flow*, Vol. 12, No. 6, 1986, pp. 861–889. doi:10.1016/0301-9322(86)90033-9

[37] Bdzil, J. B., Menikoff, R., Son, S. F., Kapila, A. K., and Stewart, D. S., "Two-Phase Modeling of Deflagration-To-Detonation Transition in Granular Materials: A Critical Examination of Modeling Issues," *Physics of Fluids*, Vol. 11, No. 2, 1999, pp. 378–402. doi:10.1063/1.869887

S. Son
Associate Editor